Undergraduate Honors Theses

Theses, Dissertations, & Master Projects

5-2017

Advancements in the Photocatalysis of Iron Complexes and the Electrocatalysis of Cobalt Complexes for Hydrogen Generation

Ryan J. DiRisio
College of William and Mary

Advancements in the Photocatalysis of Iron Complexes and the Electrocatalysis of Cobalt Complexes for Hydrogen Generation

A thesis submitted in partial fulfillment of the requirement
for the degree of Bachelors of Science in Department of Chemistry from
The College of William and Mary

By
Ryan J. DiRisio

Accepted for _____

_____

William R. McNamara, Director

_____

Kristin L. Wustholz

_____

John C. Poutsma

_____

Timothy A. Davis

Williamsburg, VA
May 02, 2017

Table of Contents

Acknowledgements

I would like to thank Dr. McNamara for his guidance, knowledge, and investment in me over the past four years as my research advisor. I received a premium education in the McNamara lab, catalyzed by you. It was fantastic coming in knowing so little about catalysis, inorganic chemistry, and how to act like a professional researcher, only to be given an opportunity to pursue my dreams of becoming a chemist under your supervision. In addition to Dr. McNamara, I want to thank the entire McNamara lab, who made the days of doing research go by fast, and who provided me the level head I desperately needed throughout my time in lab. In particular, I would like to thank Carolyn Hartley for her work, patience, and guidance throughout our time working on photochemistry experiments. I would also like to thank Jessica Armstrong and Mariah Frank for their insightful and diligent collaboration with me for our electrochemistry project. I could not have done it without you all.

I want to thank Professor Wustholz, Professor Poutsma, and Professor Davis for serving on my thesis committee. Professor Wustholz has provided me invaluable life and science advice, and has been encouraging in my pursuit of my graduate degree at the University of Washington. Professor Poutsma has deepened my love for computer science and chemistry through his computational chemistry class, and Professor Davis helped me understand it on an even more fundamental level, which was, and will continue to be, invaluable.

I want to thank my family and friends for their patience and love as well. The work load would not have been half as manageable if not for the jokes, the words of encouragement, and the relaxation that you all brought forth. You all have been grounding and caring to a degree that I cannot begin to express.

List of Figures, Tables, Equations, and Schemes

Figures

List of Appendix Figures

Chapter 1: **Introduction**

The Global Energy Crisis

Global energy consumption has increased dramatically since the beginning of the 20th century. In 2012, the amount of energy consumed was 549 quadrillion British thermal units (qBtus).[1] It is shown in Figure 1 that, by 2040, the amount will increase to 629 qBtus, a 48% increase in less than 30 years.[1] To meet energy demands in the future, fossil fuel production must increase. There are enough fossil fuels to keep up with this projected increase,[2] however there would be negative effects on the climate and the public at large through the release of harmful greenhouse gases into the atmosphere.[3-5]
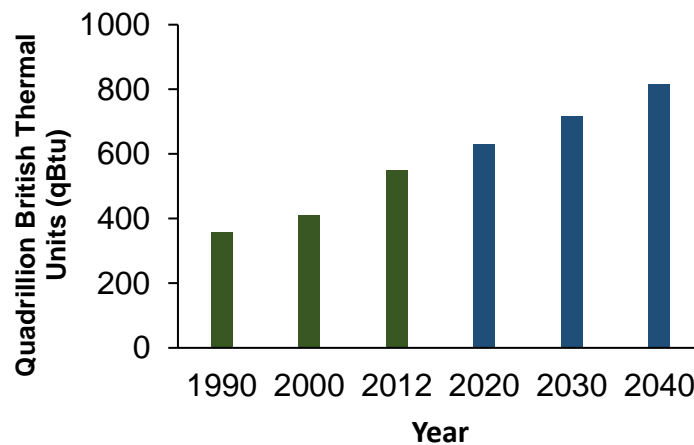
Figure 1.1: Global Energy Consumption of Energy in qBtus, historical (green) and projected (blue), over 50 years. Data courtesy of EIA.[1]

The combustion of fossil fuels (hydrocarbons) produces water and carbon dioxide. The Earth's atmosphere does not break down carbon dioxide,[2] leading to an increase in CO_2 concentration over time. As a greenhouse gas, carbon dioxide absorbs radiation from the sun, subsequently warming the Earth.[3] The effects of this warming include increased precipitation,

droughts, severe weather, and change in ocean elevation.[4] An increase of carbon dioxide in the

atmosphere also leads to an increase in dissolved carbon dioxide in the ocean, which reacts with

water to form carbonic acid.[5] Carbonic acid changes the pH of the ocean, and can adversely

affect oceanic ecosystems.[5]
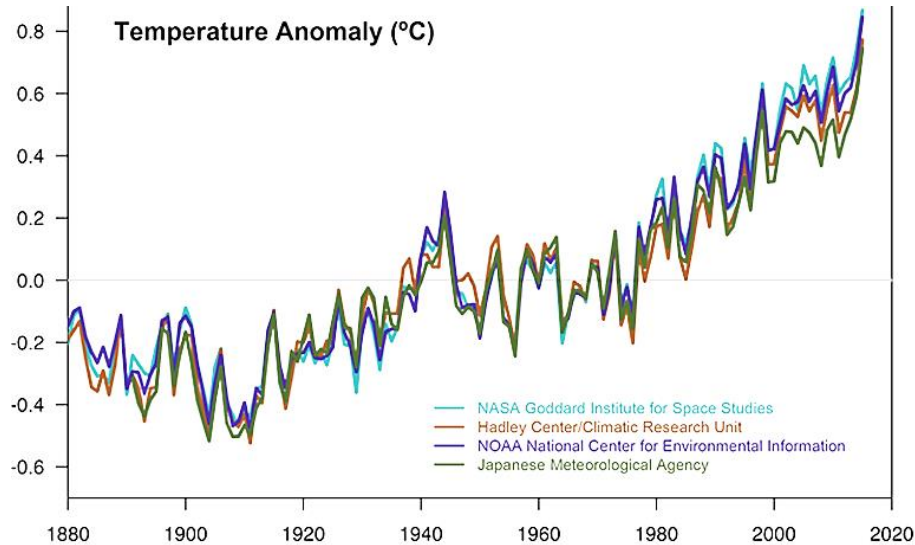
Figure 1.2. Temperature Anomaly over the past ~140 years.[6]

To prevent unnecessary harm to the environment, there has been a global effort to reduce

the amount of greenhouse gas in the atmosphere through the use of alternative energy resources.

Renewable energies such as wind, solar, and geothermal energy, along with non-renewable

energies like nuclear energy are contributing to this effort. Wind energy has become

increasingly popular.[7] However, wind is only viable in concentrated areas of the planet where

there is consistent and powerful enough wind to produce a competitive amount of energy.

Geothermal energy is more consistent, but, along with wind, can only be utilized in highly

specific regions of the world, like Iceland.[8] Nuclear reactors produce an enormous amount of

energy, but its byproducts are radioactive, and a study in 2009 showed that nuclear energy is still

not cost competitive with fossil fuels,[9] meaning that it is especially inaccessible to areas that cannot match its startup cost.

Solar energy is the most promising due to its utility in almost all regions of the world, and its lack of greenhouse gas emissions. The amount of energy that hits the earth every hour is 4.1 $\times$ (10^{20}) J.[2] Approximately 5.8 $\times$ (10^{20}) J will be consumed by the world 2020,[1] meaning that approximately 70% of the global energy supply has the potential to be harvested in one hour. Currently, solar photovoltaics are used to harvest a fraction of this large amount of energy. The cost of solar panels, which employ photovoltaic technology, has decreased significantly over the past few decades.[7] However, solar panels directly use the energy harvested from the sun,[10] which disallows for the efficient storage of energy. To this end, implementing a proper energy storage infrastructure for solar energy is paramount to the advancement of the technology.

Artificial Photosynthesis

Artificial Photosynthesis (AP) is a potential solution to the solar energy storage problem. AP takes its inspiration from traditional photosynthesis that occurs in plants. In photosynthesis, light catalyzes an oxidation of water to protons and oxygen. This oxidation releases an excited electron into photosystem II. The electron makes its way down an electron transport chain to photosystem I. After the electron is excited once more, it is transferred over to the enzyme ferredoxin-NADP+ reductase.[11a] This enzyme reduces NADP+ to NADP, which is then used to synthesize sugars that the plant uses to power itself. Research on the oxidation and reduction reactions at the beginning and end of this process have been the subject of inspiration for alternative energy development.

$$2H_2O \rightarrow O_2 + 4H+$$
$$4H+ \rightarrow 2H_2$$
$$\overline{2H_2O \rightarrow O_2 + 2H_2}$$
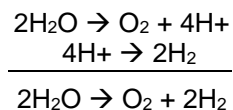
Scheme 1.1. Water splitting half reactions for hydrogen generation, incorporating the oxidation of water to oxygen gas and the reduction of protons to hydrogen gas.

In Scheme 1.1, two half reactions, one oxidation and one reduction, are used to produce oxygen and hydrogen gas. While the water splitting reaction overall is not thermodynamically favorable, a catalyst can be used to lower the overall energy required of the reaction, and the sun can be incorporated into the system to act as a provider of energy. Ideally, a device would be produced that can perform both half reactions simultaneously. However, it is advantageous to study one half reaction to decrease the cost, and increase the activity and efficiency of the final product.

The proton reduction half reaction is vital to AP, as it produces hydrogen gas that can then be used in conjunction with oxygen in a fuel cell to generate electricity, leaving only water vapor as a byproduct. This half reaction's energy can be greatly reduced with the incorporation of a catalyst. Catalyst development has become the central aspect of improving the cost-effectiveness, efficiency, and activity of the half reaction in AP systems. Colloidal platinum was one of the first effective proton reduction catalysts.[11] However, platinum is an expensive, precious metal,[11] and would not be competitive on a commercial scale.

To address the issue of cost, catalysts containing first row transition metals, such as iron,[12] nickel,[13] and cobalt,[14] have been investigated for proton reduction. Iron, nickel, and cobalt are common and cost-effective metals, making them attractive options for proton reduction.[14c] It is of great interest to investigate complexes containing these metals for active and efficient proton reduction.

In order to investigate a catalyst's activity and efficiency for proton reduction, electrochemical experiments can be performed. A particularly useful experimental technique is cyclic voltammetry (CV). Cyclic voltammetry is a technique that uses a working electrode to introduce potential into a solution while measuring the corresponding changes in current using an auxiliary electrode. A third electrode is used as an internal reference.
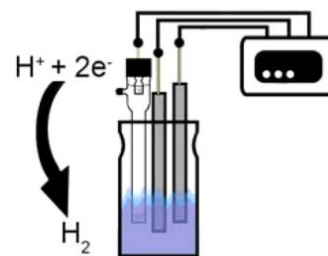
Figure 1.3. An abstraction of a cyclic voltammetry experiment. The current response is measured by a potentiostat as potential is introduced into the solution.[12c]

Using the current response of the CVs, the reduction/oxidation potential of the catalyst can be obtained. Upon addition of H^+ into the electrochemical environment, the catalyst can reduce the available protons to hydrogen. The resulting current response takes the form of an irreversible reduction peak.[15] From these current responses, information can be gathered about the catalyst, including overpotential and turnover frequency. Overpotential is the additional energy required to reduce protons to hydrogen gas past the standard, thermodynamic reduction potential,[16] and turnover frequency (TOF) is the measure of hydrogen produced per unit time.[16]
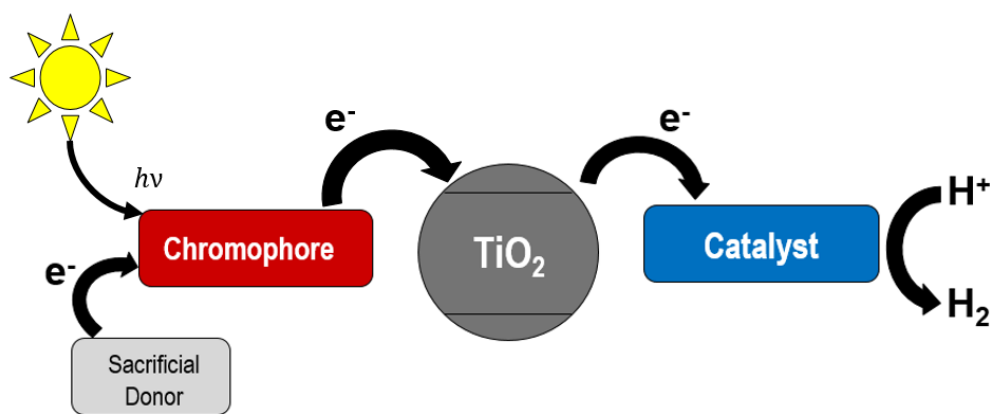
Figure 1.4: Electron Transfer process in a photocatalytic proton reduction pathway.
Once shown to be an active and efficient electrocatalyst, the catalyst of interest can be

incorporated into photochemical experimental configurations like the one in Figure 1.4. This

configuration includes a photosensitizer and a catalyst attached to a semiconductor, like TiO_2.

Light excites an electron in the chromophore, which triggers a transfer of an electron from the

valence band of TiO_2 to the conduction band. This electron is then transferred to a catalyst,

which uses the electron to reduce protons to hydrogen gas. The electron lost by the chromophore

is replenished by the sacrificial donor.

A low cost, easily synthesized, highly active, and stable transition metal catalyst is crucial

to the development of a competitive proton reduction system. With an optimized proton

reduction half reaction, as well as a cost-effective water oxidation system, a truly competitive AP

system could be manufactured to compete with fossil fuels and help solve the energy crisis at

hand. The device would be carbon neutral, and allow for the effective storage of solar energy in

the bonds of hydrogen gas.

References

1. U.S. Energy Information Administration. (2017, September). *International Energy Outlook 2016 - Chapter 1. World Energy Demand and Economic Outlook*. Retrieved 29 March 2017. From: https://www.eia.gov/outlooks/ieo/world.cfm

2. Lewis, N. and Nocera, D. Powering the planet: Chemical challenges in solar energy utilization. PNAS. 2006 103 (43) 15729-15735; published ahead of print 16 October 2006.

3. National Aeronautics and Space Administration. (2017, March 27). Global Climate Change: Vital Signs of the Planet – Facts – Causes. Retrieved 29 March 2017. From: https://climate.nasa.gov/causes/

4. National Aeronautics and Space Administration. (2017, March 27). Global Climate Change: Vital Signs of the Planet – Facts – Effects. Retrieved 29 March 2017. From: https://climate.nasa.gov/effects/

5. National Oceanic and Atmospheric Administration – PMEL Carbon Program. What is Ocean Acidification? Retrieved 29 March 2017. From: https://www.pmel.noaa.gov/co2/story/What+is+Ocean+Acidification%3F

6. National Aeronautics and Space Administration. (2017, March 27). Global Climate Change: Vital Signs of the Planet – Scientific Consensus: Earth's climate is warming. Retrieved 29 March 2017. From: https://climate.nasa.gov/scientific-consensus/

7. Next Generation Wind and Solar. 2016. International Energy Agency. Retrieved 29 March 2017. From: http://www.iea.org/publications/freepublications/publication/Next_Generation_Windand_Solar_PowerFrom_Cost_to_ValueFull_Report.pdf

8. ASKJA Energy. Geothermal Diversity. Retrieved 29 March 2017. From: http://askjaenergy.org/iceland-renewable-energy-sources/geothermal-different-utilization/

9. Massachusetts Institute of Technology. (2009). Update of the MIT 2003 Future of Nuclear Power: an Interdisciplinary Study. Retrieved from http://web.mit.edu/nuclearpower/pdf/nuclearpower-update2009.pdf

10. Eisenberg, R. (2009). Rethinking Water Splitting. Science, 324(5923), 44-45.

11. (a) Tachibana, Y., Vayssieres, L., & Durrant, J. (2012). Artificial photosynthesis for solar water-splitting. Nature Photonics, 6(8), 511-518. (b) Eckenhoff, W., & Eisenberg, R. (2012). Molecular systems for light driven hydrogen production. Dalton Transactions, 41(42), 13004-13021.

12. Connor, G, Mayer, K, Tribble, C., and McNamara, W. (2014). Hydrogen Evolution Catalyzed by an Iron Polypyridyl Complex in Aqueous Solutions. *Inorg. Chem.* 53 (11), 5408-5410. (b) Hartley, C.L., DiRisio, Ryan J., Chang, T.C., Zhang, W., & Mcnamara, W. R. (2016). Electrocatalytic hydrogen evolution by an iron complex containing a nitro-functionalized polypyridyl ligand. *Polyhedron*, 114, 133-137. (c) Cavell, A. C.; Hartley, C. L.; Liu, D.; Tribble, C. S.; McNamara, W. R. (2015). Sulfinato Iron(III) Complex for Electrocatalytic Proton Reduction *Inorg. Chem.* 54(7), 3325-3330.

13. Bianchini, C., & Fornasiero, P. (2012). A Synthetic Nickel Electrocatalyst with a Turnover Frequency above 100 000 s^{-1} for H_2 Production. ChemCatChem, 4(1), 45-46.

14. (a) Voloshin, Y., Dolganov, A., Varzatskii, O., & Bubnov, Y. (2011). Efficient electrocatalytic hydrogen production from H + ions using specially designed boron-capped cobalt clathrochelates. Chemical Communications, 47(27), 7737-7739. (b) Hu, X., Brunschwig, B., & Peters, J. (2007). Electrocatalytic hydrogen evolution at low

overpotentials by cobalt macrocyclic glyoxime and tetraimine complexes. *J. Am. Chem. Soc.* 129(29), 8988-98. (c) Marinescu, S., Winkler, J., & Gray, H. (2012). Molecular mechanisms of cobalt-catalyzed hydrogen evolution. *Proc. Nat. Acad. Sci. U.S.A.,* 109(38), 15127-31.

15. Fourmond, V., Jacques, P., Fontecave, M., & Artero, V. (2010). H_2 Evolution and Molecular Electrocatalysts: Determination of Overpotentials and Effect of Homoconjugation. *Inorg. Chem.*, 49(22), 10338-10347.

16. Rountree, E., Mccarthy, B., Eisenhart, T., & Dempsey, J. (2014). Evaluation of homogeneous electrocatalysts by cyclic voltammetry. *Inorg. Chem.*, 53(19), 9983-10002.

Chapter II: Iron Polypyridyl Complexes for Photocatalytic Proton Reduction

Introduction

AP devices generate hydrogen using sunlight, so it is of interest to examine the activity of a catalyst in a photochemical environment.
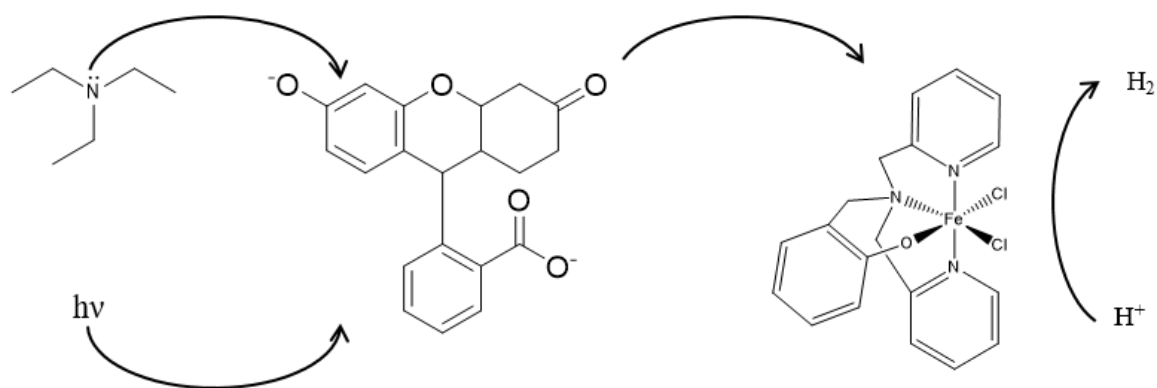
Figure 2.1: Electron transfer in a homogeneous, three-component photocatalytic proton reduction system. Here, triethylamine is the sacrificial electron donor (left), fluorescein (middle) is the chromophore, and an iron polypyridyl monophenolate complex (right) is the proton reduction catalyst.

A catalyst can be easily incorporated into a photocatalytic proton reduction environment using a homogeneous, three-component system.[1] This system includes a chromophore, a sacrificial electron donor, and a proton reduction catalyst. Ideally, light will excite the chromophore, which will prompt an electron transfer to the catalyst. This catalyst then reduces H^+ present in the aqueous solution to hydrogen gas. The chromophore cation is reduced back to its original state by the sacrificial electron donor.

Proton reduction catalysts with an iron center have been the subject of study recently due to the high abundance of the metal, as well as its natural occurrence in the hydrogenase enzyme. Hydrogenase, which performs proton reduction in plants and animals, has iron in its active site.[1] Due to the remarkable activity of the enzyme,[2] hydrogenase mimics have been the subject of

16

research in recent years. The synthesis and development of these mimics has led to incorporation of them into light-driven proton reduction systems as catalysts.[3] One potential setback is their solubility; the solubility of these complexes has even been a subject of research so that they can be incorporated into aqueous proton reduction systems.[4] In addition, the efficiency of these complexes does not match the original enzyme, since only the active site is being mimicked, not the surrounding amino acids that provide energetically favorable conditions.
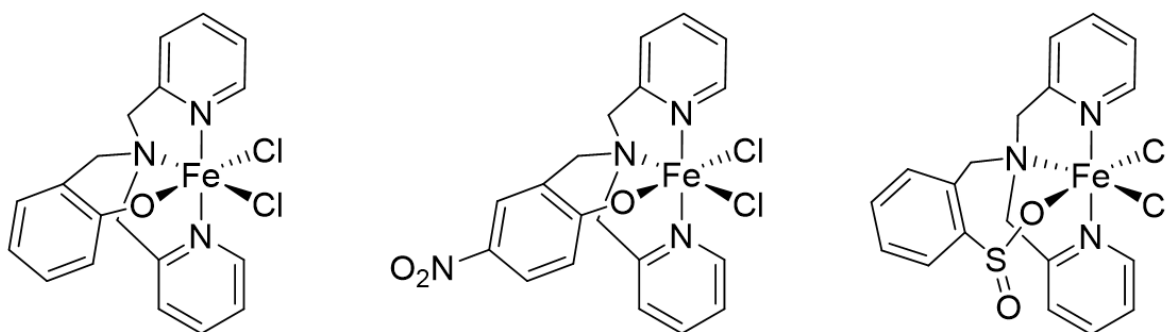
Figure 2.2: Iron polypyridyl complexes for proton reduction.

Recently, our group has reported an iron electrocatalyst[5] that was inspired by the mononuclear iron hydrogenase active site found in some organisms.[2] The catalyst was both stable and active in aqueous solutions.[5] In addition to this catalyst, two other derivatives of the catalyst have been reported.[6,7] The first derivative aims to decrease the overpotential of the catalyst by functionalizing the ligand with an electron withdrawing group on the phenolate moiety, pulling electron density away from the metal center.[6] The other replaces the phenolate with a sulfinate group, which hypothetically increases lability and therefore activity of the overall complex.[7] These complexes have all shown promise as active and efficient iron electrocatalysts for proton reduction:[5-7] the original, non-substituted complex was stable and

active in aqueous solutions, which is important for integration into aqueous photocatalytic systems,[8] the nitro-substituted complex exhibited a decrease in overpotential by 360 mV from the original complex, and the sulfinato complex had a 230% increase in catalytic activity from the original (for an explanation of overpotential and catalytic activity in the form of turnover frequency, see Chapter I, page 12 and Chapter III, page 56-59).[5-7] Since the catalysts exhibited active and efficient electrocatalytic activity, it was of interest to assess the hydrogen generation activity of these complexes in a photochemical context.

In this chapter, the three previously-reported iron complexes will be investigated for photocatalytic proton reduction. The photochemical parameters, including the concentration of each component, the choice of sacrificial donor and chromophore pairings, and the pH will be optimized to measure the ideal catalytic activity of the complexes. The robustness of the catalysts will be investigated by examining hydrogen generation over time. Additionally, the photochemical mechanism of proton reduction will be investigated, including the percentage of photons contributing to hydrogen generation (quantum yield), and the role the chromophore plays in the catalytic mechanism.

Experimental
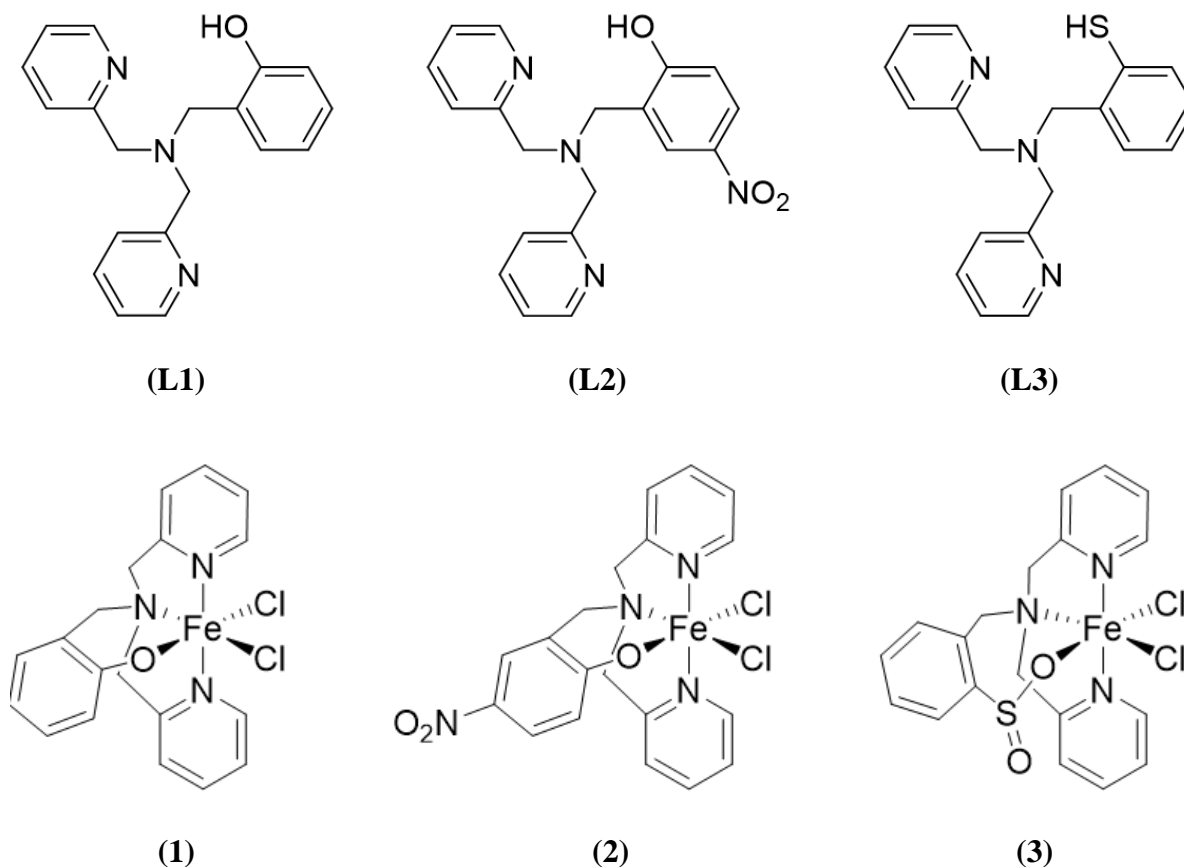
Figure 2.3. Ligands **L1** (Top Left)**, L2** (Top Middle)**, and L3** (Top Right). Complexes **1** (Bottom Left)**, 2** (Bottom Middle)**, and 3** (Bottom Right).

Materials and Methods

All experiments were performed under an atmosphere of argon unless noted otherwise. For the synthesis of **L1** and **1**, salicylaldehyde, bis(pyridine-2-ylmethyl)amine, and iron trichloride hexahydrate were purchased from Fischer Scientific. For **L2** and **2**, 2-Hydroxy-5-nitrobenzaldehyde was purchased from Alfa Aesar. Bis(pyridin-2-ylmethyl)amine was purchased from Aldrich. Iron trichloride hexahydrate and potassium hydroxide were purchased from Fisher Scientific. For the synthesis of **L3** and **3**, iron trichloride hexahydrate, thiosalycylic acid,

sulfuric acid, bromopropionitrile, phosphorus tribromide, bis(pyridine-2-ylmethyl)amine, sodium methoxide, and triethylamine were purchased from Fischer Scientific. Tetra-n butylammoniumhexafluorophosphate (98%), was purchased from Acros Organics.

Instrumentation

^{1}H and ^{13}C spectra were gathered from Agilent 400MR DD2 Spectrometer in Fourier transform mode. Chemical shifts are based on residual solvent. Elemental analysis for **1** was performed by Atlantic Microlab, Norcross, GA 30071. Elemental analysis for **2** and **3** were performed by the CENTC Elemental Analysis Facility at the University of Rochester, funded by NSF CHE 0650456. Mass spectrometry of **1** was performed through positive electrospray ionization on a Bruker 12 Tesla APEX-Qe FTICR-MS using an Apollo II ion source. Mass spectrometry of **2** was performed by the Cosmic Facility at Old Dominion University in Norfolk, VA.

X-Ray Diffractometry

Single crystals were mounted on glass fibers and data for **1** and **2** were collected with graphite monochromated Cu Kα radiation (λ = 1.54187 nm) on a Bruker-AXS three-circle diffractometer using a SMART Apex II CCD detector. Crystal structures were solved via direct methods and refined using SIR2014 and SHELXL-2014/7

Single crystals of **3** were mounted on glass fibers and data was collected with graphite monochromated Mo Kα radiation on a Bruker SMART Apex II CCD platform diffractometer. The structure was solved using SIR20114 and refined using SHELXL 2014/7. The space group P43 was determined based on CSD statistics and having solved the structure in space groups P1 and P21 and noting the higher symmetry visually and via the Addsym function of program

Platon. A direct-methods solution was calculated, which provided most non-hydrogen atoms

from the E-map. Full-matrix least-squares/ difference Fourier cycles were performed, which

located the remaining non-hydrogen atoms. Non-hydrogen atoms were refined using anisotropic

63 displacement parameters, and hydrogen atoms were placed in ideal positions and refined as

riding atoms with relative isotropic displacement parameters.

Synthesis

N-(2-hydroxybenzyl)-N,N-bis(2-pyridylmethyl)amine (L1). Under argon, 10 mmol of

dipicolylamine was dissolved in 10 mL of methanol, and 10 mmol of salicylaldehyde are

dissolved in 50 mL of methanol. The dipicolylamine was added to the solution of

salicylaldehyde, and then 3 drops of glacial acetic acid were added, followed by 5 mmol sodium

cyanoborohydride dissolved in 5 mL of methanol under argon. The solution was left to reflux

for one hour. After reflux, the ligand was left to stir overnight. The solution was then brought

under acidic conditions (pH = 4) using 1 M HCl. The solvent was then almost completely

removed. The solution was then neutralized with 25 mL of saturated Na_2CO_3 and was extracted

3x with 75 mL $CHCl_3$. After extraction, the organic layer of interest was dried using Na_2SO_4

and then filtered through celite. After solvent was removed the product was a yellow/orange oil,

which was then run through a silica gel column at 99:1, then 19:1, then 9:1 CH_2Cl_2:CH_3OH.

After removing the solvent once more the product was a yellow/orange oil (% Yield = 59). [1]H

NMR, $CDCl_3$: ∂ 8.49 (d, 2H), 7.57 (t, 2H), 7.29 (d, 2H), 7.10 (m, 3H), 7.00 (d, 1H), 6.84 (d, 1H),

6.70 (t, 1H), 3.81 (s, 4H), 3.73 (s, 2H).

Fe(L1)Cl$_2$ (1). 1's synthesis followed a modified literature procedure[9]. **L1** was dissolved in

methanol along with triethylamine under argon. Iron trichloride hexahydrate was then added to the solution, and there was a color change from yellow/orange to dark blue. After stirring for 1 hour, there was dark blue precipitate in the reaction vessel. The solution was then filtered, and the filtrate was discarded. The crystals were washed with 10 mL of methanol 3x (74% Yield). After the product was obtained it was crystallized via slow diffusion. The crystals were dissolved in CH_2Cl_2 and hexanes were layered on top of the solution. Blue crystals were then harvested. m/z for $C_{19}H_{18}N_4O_3H^+$ expected = 395.048233, found = 395.048640. Anal. Calc. for **1** monohydrate $FeC_{19}H_{18}N_3Cl_2 \cdot H_2O$: C, 50.8; H, 4.49; N, 9.36%. Found: C, 50.66; H, 4.18; N, 9.13%.

2-((bis(pyridin-2-ylmethyl)amino)methyl)-4-nitrophenol) (L2). 3 mmol of dipicolylamine, and 3 mmol of 5-nitrobenzaldehyde are dissolved in 50 mL of methanol. 3 drops of glacial acetic acid are added, followed by 3 mmol sodium cyanoborohydride. The solution was left to reflux for 1 hour. After reflux, the ligand was left to stir overnight. The solution was then brought under acidic conditions (pH = 4) using 1M HCl. The solvent was then almost completely removed, and was then neutralized with saturated Na_2CO_3. An extraction was performed using $CHCl_3$. After extraction, the organic layer of interest was dried using Na_2SO_4 and then filtered through celite. After solvent was removed the product was a yellow/orange oil, which was then run through a silica gel column at 9:1 $CH_2Cl_2:CH_3OH$. After removing the solvent once more the product was a red oil (62% Yield). ^{1}H NMR (CDCl3): δ 8.58 (d, 2H), δ 8.12 (d, 1H), δ 8.05 (2, 1H), δ 7.66 (t, 2H), δ 7.30 (d, 2H), δ 7.21 (t, 2H), δ 6.95 (d, 1H), δ 3.93 (s, 4H), δ 3.85 (s, 2H). ^{13}C NMR (CDCl3): δ 164.27, δ 157.71, δ 148.69, δ 139.68, δ 137.06, δ 126.54, δ 125.61, δ 123.52, δ 123.08, δ 122.41, δ 117.17, δ 58.67, δ 56.10. m/z for

$C_{19}H_{18}N_4O_3H^+$ expected = 351.15, found = 351.15.

Fe(L2)Cl₂ (2). The synthesis followed a modified literature procedure[10]. **L2** was dissolved in methanol along with triethylamine under argon. Iron trichloride hexahydrate was then added to the solution, and there was a color change from yellow/orange to dark purple. After stirring for 1 hour, there was dark purple precipitate in the reaction vessel. The solution was then filtered, and the filtrate was discarded. The crystals were washed with 10 mL of methanol 3x (41% Yield). After the product was obtained it was crystallized via slow diffusion. The crystals were dissolved in CH_2Cl_2 and diethyl ether was layered on top of the solution. Purple crystals were then harvested. m/z for $C_{19}H_{17}Cl_2FeN_4O_3Na^+$ expected = 497.991934, found = 497.992060. Anal. calc. for **2**: C, 47.83; H, 3.80; N, 11.74. Found: C, 47.77, H, 3.83, N, 11.90.

O-mercaptobenzyl alcohol. 20 mmol of thiosalycylic acid was dissolved in 75 mL of diethyl ether under argon. $LiAlH_4$ was added under argon. The solution was left at room temperature to stir for 1 hour. The solution was placed in an ice bath, and 4.0 mL of DI H_2O was added dropwise. After, 20 mL of 10% H_2SO_4 was added. The solution was left to stir for 48 hours at room temperature. The solution was then extracted using diethyl ether 3x30 mL). The organic layer was collected and dried using $MgSO_4$. The solution was then evaporated. The product formed was a yellow oil (82% yield). The ^1H peaks matched those reported in literature[11].

3-(2-hydroxymethylphenylsulfanyl)propionitrile. 7.12 mmol of o-mercaptobenzyl alcohol was dissolved in 15 mL of ethanol. The solution was then degassed with argon. 10 mmol of NaOH dissolved in 5 mL of H_2O was then added. In addition, 10 mL of ethanol was added to solution.

7.1 mmol of bromopropionitrile was added dropwise under argon and the mixture was stirred for 5 hours at room temperature. The solution was then filtered and the solvent was evaporated. A yellow, oily solution was left over. The solution was then dissolved in 25 mL of diethyl ether. The solution was washed with 10 mL of 5% NaOH and 10 mL of H_2O. $MgSO_4$ was then added to dry the solution, and the solvent was evaporated once more, yielding the product, which was a white solid. The NMR spectra (^1H and ^{13}C) matched those reported in literature[11].

3-(2-bromomethylphenylsulfanyl)propionitrile. 1.473 mmol of 3-(2-hydroxymethylphenylsulfanyl)propionitrile was dissolved in 22 mL of dichloromethane and degassed with argon. This solution was transferred to a Schlenk flask, and the solution was immersed in an ice bath. 0.6 mmol of 1.0 M PBr$_3$, under argon, was added dropwise to the Schlenk flask. The solution was stirred for 4 hours at room temperature. The solution was then washed with 10 mL of 10% NaOH and 10 mL of H_2O. The solution was then dried with $MgSO_4$ and then the solvent was evaporated to yield a clear yellow oil (80% yield). The NMR spectra (^1H and ^{13}C) matched those reported in literature[11].

3-(2-propionitrilemercaptobenzyl)-N,N-bis(2-pyridylmethyl)amine. 1.335 mmol of 3-(2-bromomethylphenylsulfanyl)propionitrile was dissolved in 20 mL of ethyl acetate and degassed with argon. The solution was moved to a Schlenk flask, to which a degassed solution of 1.671 mmol dipicolylamine in 15 mL of ethyl acetate was added. Then, 7.17 mmol of trimethylamine in 15 mL of ethyl acetate was added and the solution was stirred for 72 hours. The solution was filtered and the solvent was evaporated to yield the product. The product was further purified via silica gel column in 7:3 ethanol:ethyl acetate (59% yield). The NMR spectra (^1H and ^{13}C)

matched those reported in literature[11].

N-(2-mercaptobenzyl)-N,N-bis(2-pyridylmethyl)amine (L3) Ligand 3 was synthesized using a modified literature procedure[11]. 0.112 mmol of N-(2-propionitrilemercaptobenzyl)-N.N-bis-(2-pyridylmethyl)amine was dissolved in 10 mL of methanol and degassed with argon. In a Schlenk flask, the N-(2-propionitrilemercaptobenzyl)-N.N-bis-(2-pyridylmethyl)amine solution was combined with 0.180 mmol of sodium methoxide. This solution was refluxed for 72 hours. The result was a clear, amber solution. This solution was filtered and the solvent was removed to yield a solid. This solid was then extracted by dissolving it in 13 mL of dichloromethane and adding 13 mL of DI H_2O to quench any excess sodium methoxide. The organic layer was orange-brown and was collected. The solvent was removed to yield the product, a brown oil. The ligand was purified via silica gel column, using 9:1 dichloromethane:methanol solution. Ligand 3 was collected as a brown oil (45% yield). The NMR spectra (^1H and ^{13}C) matched those in literature[11]. m/z for $(C_{19}H_{19}N_3S)H^+$ expected = 322.137245, found = 322.137527.

Fe(L3)Cl2 (3). 0.312 mmol of ligand 3 was dissolved in 10 mL of methanol along with 0.312 mol of triethylamine, which was then degassed with argon. 0.312 mmol of iron trichloride hexahydrate was dissolved in 10 mL of methanol and degassed with argon. The two solutions were combined, which yielded a brown solution with a precipitate. The resulting solution was left to stir for 12 hours at room temperature. Afterwards, the solution was filtered. The filtrate's solvent was then removed, yielding a solid. This solid was recrystallized in dichloromethane to purify the product. The product was collected as a dark solid (71% yield). Crystals for diffraction were grown via slow diffusion. The solid was dissolved in acetonitrile, and diethyl

ether was layered on top. HR MS: m/z for $(C_{19}H_{18}Cl_2FeN_2O_2S)Na^+$ expected $= 500.973841$, found $= 500.974354$. Anal. Calc. $FeC_{19}H_{18}Cl_2N_2O_2S$: C, 47.63%; H, 3.79%; N, 8.77%. Found: C, 47.77%; H, 4.12%; N, 8.44%.

Photochemistry Experiments

Quenching Experiments

Catalyst Quenching (oxidative quenching)

A 4.0 mM fluorescein in ethanol stock solution was prepared. In addition, 0.8 mM catalyst stock solutions in ethanol each were prepared. 7.5 µL of fluorescein stock solution was added to 3 mL of a 1:1 water:ethanol solution at pH $= 12.5$. This solution was degassed with argon in an air free cuvette for 15 minutes after being wrapped in aluminum foil. Catalyst from the stock solution was also degassed with argon for 15 minutes. These solutions were kept under an atmosphere of argon throughout the experiment by using argon balloons. After a base scan of the fluorescein solution, emission spectra were gathered for incremental 10 µL additions of catalyst. Fluorescence was probed by exciting the solution at 430 nm. Additions went up to 80 µL for each catalyst unless stated otherwise. The experiment was repeated for each catalyst. From the spectra, peak intensities were measured and Stern-Volmer plots were generated.

Sacrificial Donor Quenching (reductive quenching)

Reductive quenching by triethylamine was performed almost identically to the procedure above. Instead of a catalyst stock solution, triethylamine was degassed with argon and added to the fluorescein solution. Instead of 10 µL additions of catalyst, 30 µL additions of triethylamine were injected, and additions went up to 400 µL. From the spectra, peak intensities were

measured and Stern-Volmer plots were generated.

Hydrogen Evolution over Time Studies

Samples for the time studies were prepared in 16.0 mm x 125.0 mm glass test tubes. 20 µL of 0.4 mM stock catalyst solution in CH_3CN, 1.8 mL of 4.0 mM stock fluorescein in ethanol, 180 µL of ethanol, and 2.0 mL of 10% v/v TEA:H_2O were added into the test tube. Micro-size stir bars were also added to the test tubes. The test tubes were then capped with air tight septa and degassed with argon for 15 minutes after being secured with copper wire. After degassing, 1.0 mL of argon was removed from the test tube using a Hamilton gastight syringe, and 1.0 mL of methane was injected into the test tubes. The methane acted as an internal standard for GC measurements. The test tubes were then placed in a 6-test tube, custom-made holder. This holder was spun by a small motor (3 revolutions/minute) above a stir plate. The test tubes were removed from their foil and were surrounded by LEDs attached to a large beaker (λ = 520 nm, P = 1.8 mW). Green LEDs were chosen since many chromophores absorb light in this region. A fan was placed nearby to cool down the LEDs throughout the experiment. Throughout the experiment, 100 µL headspace samples were taken from the test tubes and injected into a GC to measure the amount of hydrogen generated over time.

Hydrogen evolution over time using local pond water

Water was collected from Lake Matoaka on the campus of The College of William & Mary in Williamsburg, VA. The water was refrigerated in sealed 60 mL jars until used for experiments, at which point they were returned to room temperature. The pond water was purified by gravity filtration. Test tubes were prepared identically to the procedure outlined above. However, the

DI H_2O that was added into the solution with TEA was replaced by the filtered pond water.

Quantum Yield Studies

A test tube was prepared per the procedure outlined by the hydrogen evolution over time studies. A Coherent Fieldmate Laser Power Meter measured the power from the LEDs and the power of light leaving the sample. This was done at the beginning of the experiment and after 24 hours. The difference in power was used to calculated the quantum yield. See Appendix A for the equations and sample calculations

GC Calibration

Two 500 mL roundbottom flasks were put under vacuum. One was then filled with CH_4 and the other with H_2. Both were sealed with airtight septa. Additionally, a test tube was prepared with 2.0 mL of acetonitrile and 2.0 mL of DI H_2O. The solution was then covered with an air tight septa and secured with a copper wire.
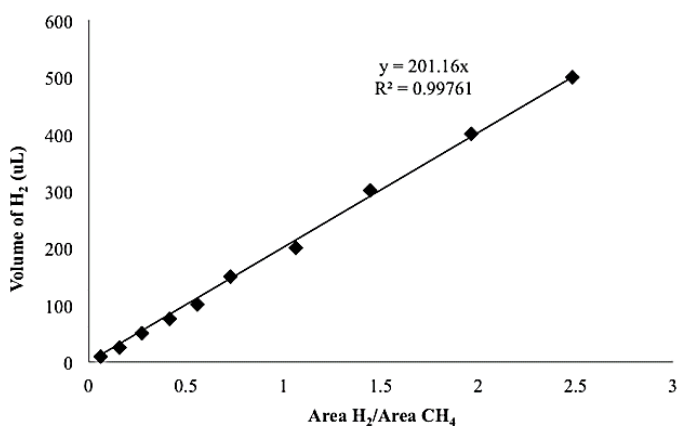

Figure 2.4. Calibration curve for quantification of hydrogen produced using GC analysis.

This test tube was then degassed with argon for approximately 15 minutes. A Hamilton gastight syringe was then used to extract 1.0 mL of gas from the test tube. Then, 1.0 mL of CH_4 was injected into the solution. The CH_4 was added as an internal standard for GC analysis. Then,

28

various injections of H_2 were made into the test tube, from 10 μL to 500 μL. Samples of 100 μL

of the headspace of the test tube were injected into the GC to get the ratio of H_2 to CH_4. The

ratios were plotted against the volume of H_2 injected into the test tube to calculate the amount of

hydrogen produced in the hydrogen evolution experiments, seen in Figure 2.4.

Results and Discussion

The complexes were synthesized and characterized according to literature procedure.[5-7] As an additional level of characterization, UV-Vis spectra were taken to elucidate the transition states of the complex (see Appendix A). Absorption events occurred at ~360 nm for all complexes, which correlate with ligand pπ to iron dσ* transitions.[12,13] Additionally, absorption events in the 500-600 nm range correlate with ligand pπ to iron dπ* transitions.[12,13] Therefore, both absorption events indicate metal to ligand charge transfer in **1-3**. [12,13]

After structural elucidation and characterization, it was of interest to measure the photocatalytic activity of the complexes. A standardized metric was used to quantify the amount of hydrogen produced. Turnover number (TON), which are the moles of hydrogen produced per mole of catalyst, is a useful metric for comparing catalysts. The higher the TON, the more active the photocatalytic system. Over time, TON should increase linearly if the system is producing hydrogen consistently. To maximize turnovers, the photocatalytic system needed to be optimized. This includes varying each component of the system.

To start the optimization process, different chromophores were paired with the catalysts to observe activity. Three chromophores were chosen as potential photosensitizers due to their effectiveness and stability in previous AP systems. Ru(bpy)$_3$$^{3+}$ is the most stable of the three due to its low chance of bleaching.[14] However, Ruthenium is costly, and could potentially make the AP system non-competitive. Fluorescein and Eosin Y are both organic chromophores, and are quite inexpensive. Fluorescein is a singlet emitter, and can be used in comparison with Eosin Y. Eosin Y has functionalized bromines, which means it is a triplet emitter. In addition to excited states, eosin Y can operate at a more neutral pH, while fluorescein operates optimally at a more basic pH.[15] However, organic chromophores are known to decompose upon irradiation in

solution.[16] These diverse, and previously used, chromophores offer elucidation of optimal conditions in a large pH range.

In preliminary studies, which measured the amount of hydrogen generated after 12 hours using various sacrificial donors/chromophore pairings (see Appendix A), fluorescein was the most adept at producing hydrogen in the three-component system. This is most likely the case because fluorescein has proven to be a highly reducing chromophore in photocatalytic systems that employ catalysts with similar electrochemical reduction potentials of **1-3.**[5-8,16,17] Eosin Y and Ru(bpy)$_3{}^{3+}$ both produced hydrogen in their corresponding systems with few or no catalytic turnovers.

In addition to chromophore choice, it was important to pair a proper sacrificial donor with the best photosensitizer. Triethylamine (TEA), triethanolamine (TEOA), and ascorbic acid were paired with each of the chromophores to optimize turnover numbers as well. Pairing fluorescein with TEA yielded the highest rate of hydrogen generation. TEA is a promising sacrificial electron donor because it has been paired with fluorescein before, and it has been shown to effectively quench fluorescein in previous systems.[17] TEA and fluorescein work well together due to high performance at a more basic pH.[17] TEA becomes protonated at lower pH, and makes it a less effective sacrificial donor.[17]

Adjusting the Parameters of the Photocatalytic System

To maximize hydrogen generation in the photocatalytic system, pH, [chromophore], and [catalyst] are independently varied to find the optimal conditions. In terms of pH, the system performed optimally at very basic conditions. Optimally, the system generated the most amount of hydrogen at pH = 12.5. Other than TEA becoming less effective at lower pH, as mentioned

31

above, fluorescein would exist in more protonated states, which would render it less soluble in our system.
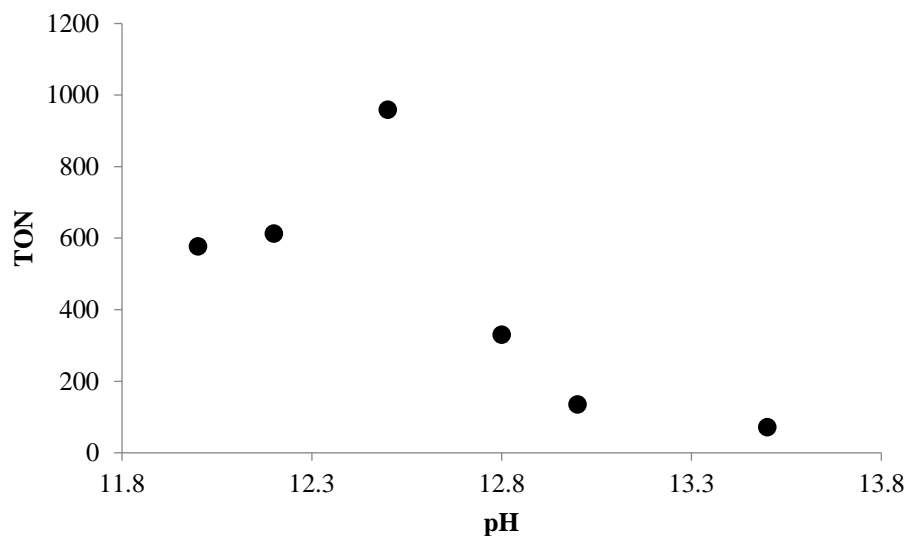

Figure 2.5. Varying pH and measuring subsequent TONs in a system with **1**.

The concentration of fluorescein was varied in the system to optimize photocatalytic activity as well. The optimal fluorescein concentration was 1.9 mM. There was a general trend upwards regarding TON vs. [fluorescein], however, there seems to be a limit to this at 1.9 mM. This limit is most likely due to self-quenching of fluorescein by neighboring ones, leading to a lower level of activity.
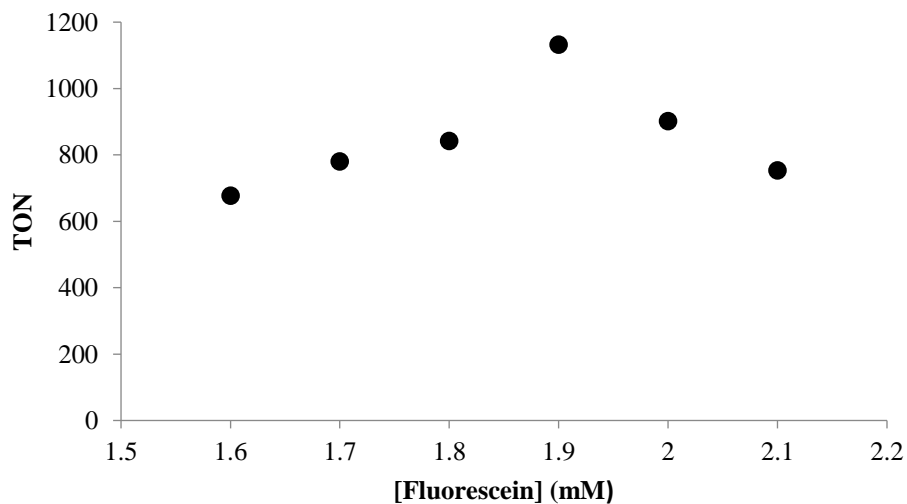

Figure 2.6. Varying [fluorescein] and measuring subsequent TONs in a system with **1**.

Varying the concentration of catalyst in the system was crucial to optimizing catalytic activity as well. It was found that, generally, lower concentrations of catalyst were optimal for hydrogen generation. Specifically, the optimal concentration of catalyst in a system was 2 µM. Low concentrations of catalyst has been shown in literature to be a trend in transition metal complex photocatalytic systems.[17,18] This is due to a limiting factor in the system in which adding more catalyst does not produce more hydrogen, thus decreasing the TON. **2** and **3** were both optimized in the same way, only minorly differing in results with respect to the [catalyst] (See Appendix A).
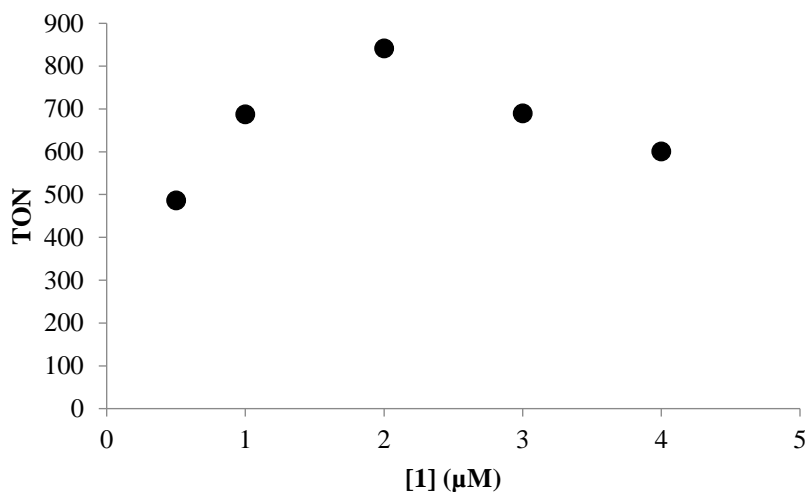

Figure 2.7. Varying [**1**] and measuring subsequent TONs.

To measure the stability and hydrogen generation of the optimized systems over time, the headspace of test tubes containing each catalyst were measured for hydrogen at the 1, 3, 6, 12, and 24-hour point via gas chromatography. Based on the electrocatalytic data, it was hypothesized that, because of their respective i_c/i_p and overpotentials, **2** would be the most stable catalyst, linearly generating hydrogen for the longest period, **3** would produce the most

amount of hydrogen, but be the least robust catalyst, and **1** would fall in between.
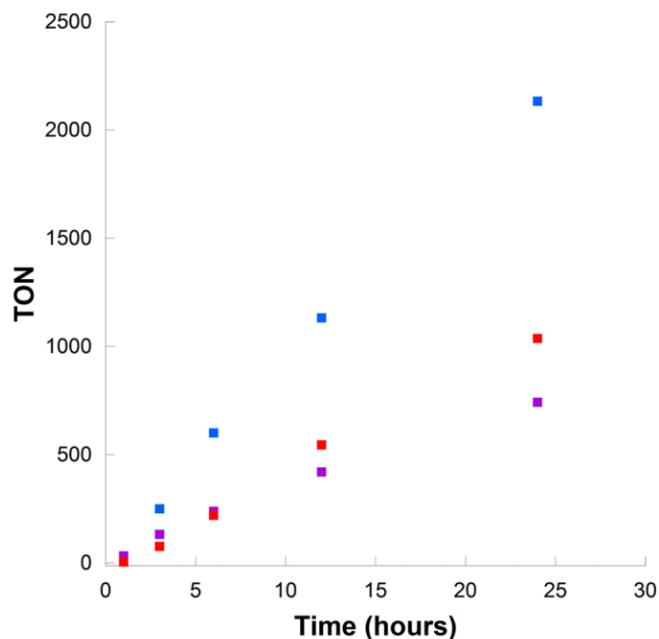

Figure 2.8. Hydrogen Generation of **1** (blue), **2** (red), and **3** (purple) over 24 hours.

Interestingly, **1** showed the highest amount of hydrogen produced in a 24-hour period at ~2100 TON. **2** showed the second highest at ~1030 TON, and **3** was last at ~740 TON. The results were not as hypothesized, since **3** should hypothetically produce hydrogen at the highest of turnovers, if the electrocatalytic data reflected an accurate comparison. **3** produced hydrogen linearly at a faster rate than 2 initially until hour 6, at which point it decreases in activity (See Figure 2.8). To better understand the activity of **3** relative to the others, it was of interest to elucidate the photochemical pathway of our system.

Mechanistic Insights

The photocatalytic system containing **3** did not perform as hypothesized. Therefore, finding the limiting factor of the system was important to understanding its underperformance, whether that be the catalyst or the chromophore. To understand the limiting factors of our

photocatalytic system, fluorescein addition experiments were performed. After 24 hours, typically, the system's rate of hydrogen generation deviates from linearity. Additional fluorescein was injected after 24 hours of hydrogen generation using **1**. A headspace sample was taken 1 hour after injection to observe a possible change in linearity. Consequently, linearity was restored for approximately 10 hours. This was repeated at hour 35, and a return to linear hydrogen generation was shown once more (see Appendix A). The results strongly suggest that fluorescein was the limiting factor of the photocatalytic system at 24 hours for **1**. Further studies are needed to investigate the limiting factor past 24 hours with **2** and **3**.

Fluorescein is a large contributor to limiting hydrogen generation. Because of this, it was of interest to explore the decomposition of fluorescein in solution. To explore the decomposition of fluorescein, it was necessary to determine the mechanism through which fluorescein was reducing the catalyst. There are two pathways through which fluorescein can deliver an excited electron to the iron complex: these are referred to as the reductive and oxidative pathways.
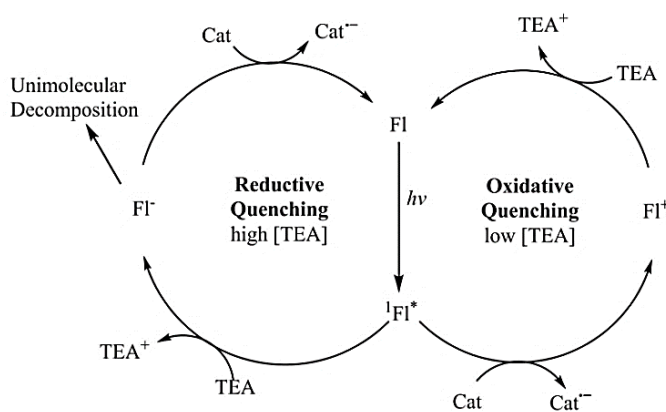
Figure 2.9. Photochemical quenching pathways for fluorescein.[19] Note the reductive quenching pathway leads to decomposition.

The pathways are dependent on the concentration of the sacrificial donor. In the oxidative pathway, fluorescein is excited by light, and the excited electron is transferred to the

catalyst, oxidizing the chromophore. Afterwards, the fluorescein cation is reduced by the sacrificial donor TEA back to its original state. In the reductive pathway, fluorescein is excited with light, and then TEA reduces fluorescein to make it Fl$^-$. Fl$^-$ is an unstable species that may undergo decomposition in our system.[17] This excited anionic species then transfers its excited electron over to the catalyst, returning to its electronically-neutral ground state. Because of the excited fluorescein anion's instability, the oxidative pathway is favorable.

To examine if the oxidative pathway is taken, quenching experiments were performed. These experiments allow for the elucidation of quenching rates via the Stern-Volmer relationship:

$$\frac{I_0}{I} = k[Q] * \tau + 1$$

Where I_0 is the initial intensity, I is the newly measured intensity, Q is the concentration of quencher, and τ is the lifetime of the excited state. A quenching rate of fluorescein constant k can then be calculated for TEA, **1**, **2**, and **3**. The results can be seen in Table 1. The results showed that TEA has a faster quenching rate than **1**, **2**, and **3**, suggesting that the reductive quenching pathway was used most frequently by all of the catalysts. In addition to this, **3**'s quenching rate was the lowest of the three, implying that fluorescein decomposed more readily in experiments containing **3**. This is supported by the previously mentioned observation of the deviation from linearity in the 24-hour study.

Quencher	Quenching Constant ($M^{-1}s^{-1}$)	Quenching Rate (s^{-1})
TEA	$2.29 \times (10^8)$	$8.24 \times (10^7)$
1	$2.26 \times (10^{10})$	$4.41 \times (10^4)$
2	$3.13 \times (10^{10})$	$6.40 \times (10^4)$
3	$5.51 \times (10^9)$	$1.20 \times (10^4)$

Table 2.1. Quenching constants and subsequent quenching rates for **1**, **2**, **3**, and TEA.
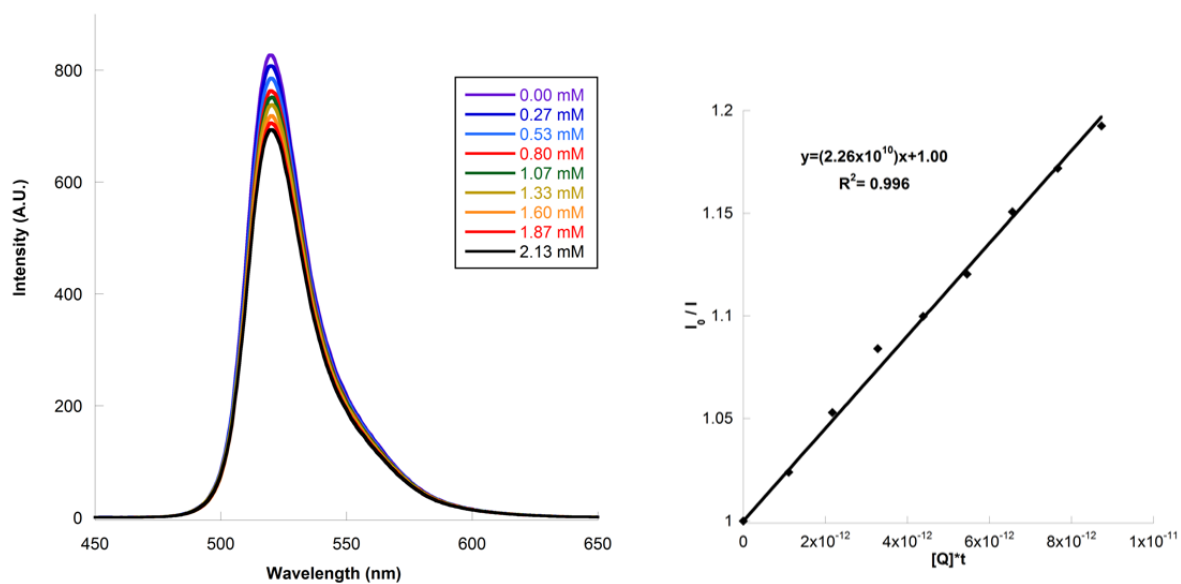
Figure 2.10. Emission spectra of the quenching of fluorescein with **1** (left). Stern-Volmer relationship (right).
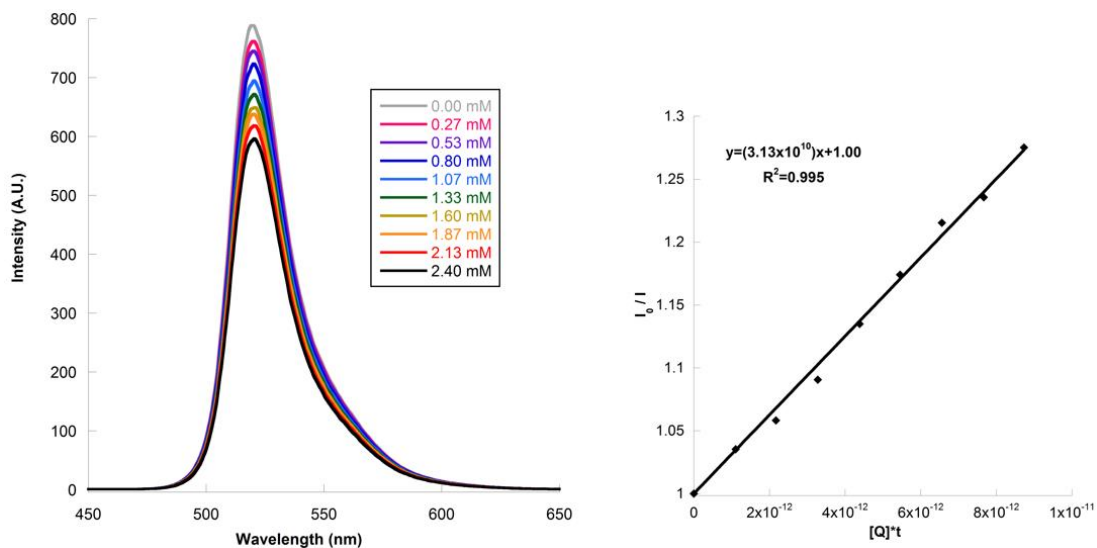

Figure 2.11. Emission spectra of the quenching of fluorescein with **2** (left). Stern-Volmer relationship (right).
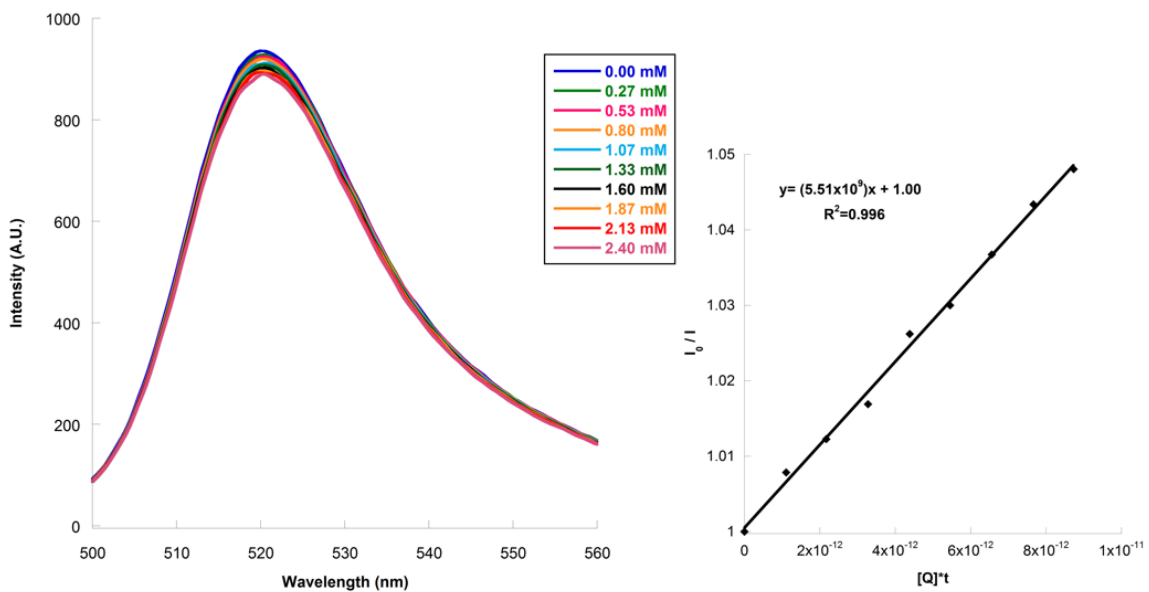
Figure 2.12. Emission spectra of the quenching of fluorescein with **3** (left). Stern-Volmer relationship (right).
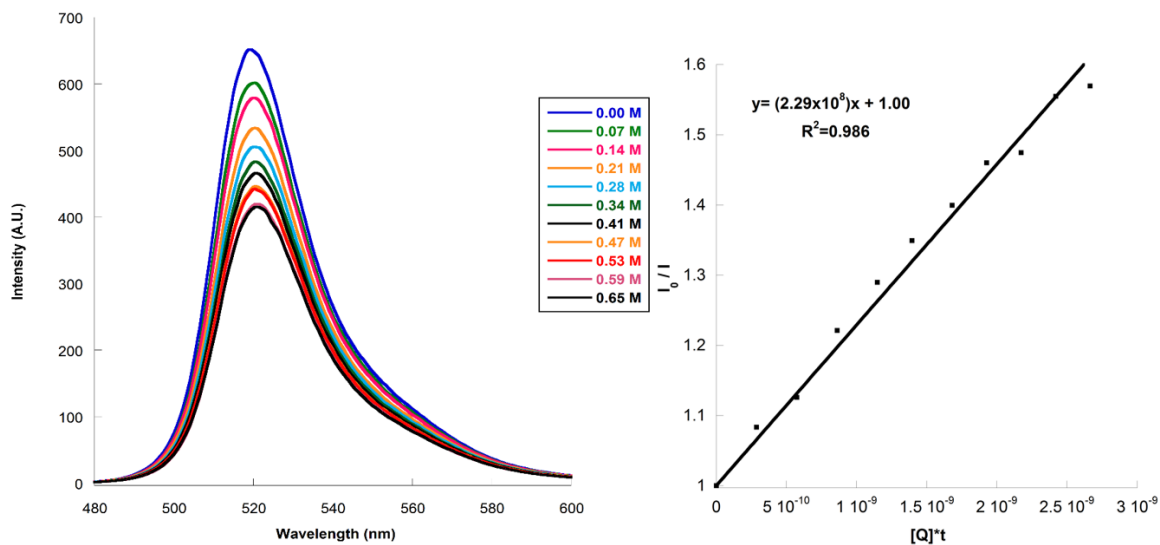

Figure 2.13. Emission spectra of the quenching of fluorescein with TEA (left). Stern-Volmer relationship (right).

In addition to investigating the photochemical mechanism of the system, calculating the photochemical efficiency of the system was also important. To investigate the ratio of photons hitting the solution versus the amount that contribute to the reduction of protons to hydrogen gas, quantum yield studies were performed. The difference in power from the LEDs and through the test tube of a hydrogen generation study is used to calculate a percentage of photons being used for hydrogen generation. It was calculated that the quantum yield of the system involving **1** was 3.1%, **2** was 3.4%, and **3** was 1.9%. A sample calculation of quantum yield was conducted in Appendix A. While the quantum yield is low, many systems of a similar nature typically only have quantum yields on the same order of magnitude as well.[18,20]

Testing the robustness of a photocatalytic system was crucial to having it be a promising and cost-effective system for proton reduction. Ideally, systems that generate hydrogen from water should not rely on distilled, lab-grade water sources. To be the most accessible energy resource, AP systems should work in systems without clean water. In order to bring our system into this context, we used local pond water on The College of William & Mary's campus to test the toughness of our system. Water was gathered from Lake Matoaka, and stored in a refrigerator until the hydrogen generation experiments were performed. The water was brought to room temperature, and it was filtered using filter paper to remove large particulate matter. The water was then used in our hydrogen generation over time studies instead of the traditional, deionized water. **1** was used for this experiment, as it generated hydrogen at the highest TONs.
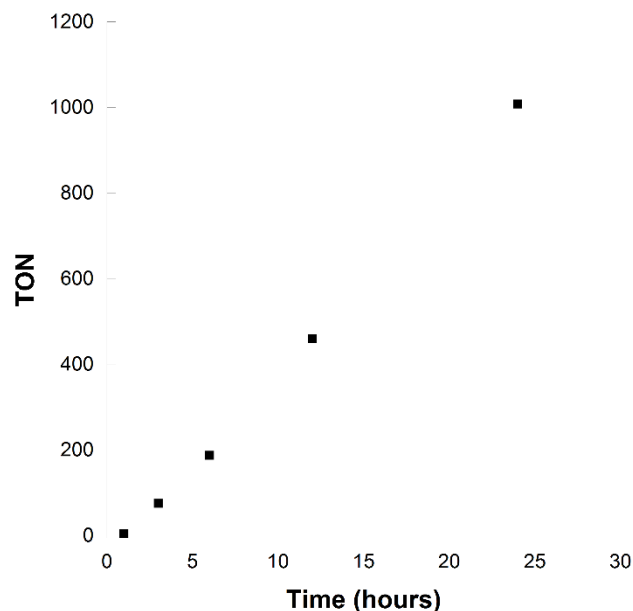
Figure 2.14. Hydrogen evolution over time study using water from Lake Matoaka and **1**. The points show a linear generation of hydrogen over time for 24 hours, operating at about half of the activity of the optimal conditions using deionized water.

The system produces hydrogen at about half capacity for 24 hours, yielding a TON of ~1000 for **1**. This shows that our photocatalytic system is stable enough to endure water that is present with potential microbes, particulates, and salts. In addition, the system linearly produces hydrogen for 24 hours, meaning that it endures the conditions for the same amount of time as our original system.

This system that integrates water-soluble iron complexes and organic chromophores is inexpensive, robust and active. **1**'s system is believed to be the one of the most active proton reduction systems incorporating a homogeneous iron catalyst reported.[8] **1** generated hydrogen with very high (~2100) turnovers, while **2** and **3** generated hydrogen with high turnovers (~1030 and ~740, respectively) as well. The quenching pathway was proven to be unfavorable, and future studies can be done to examine the role of the concentration of TFA in the quenching mechanism. The quantum yield studies showed that the systems are on par with the current state

of photocatalytic hydrogen generation systems. The system lasts for 24 hours, and lasts longer if additional fluorescein is added.

Due to the stability and activity of this photocatalytic system, it will be of interest in the future to implement other iron catalysts into photocatalytic systems for hydrogen generation. This system shows that a cost-effective, noble metal free hydrogen generation system is a realistic goal for AP. With a cost-competitive and enduringly stable and active system for light driven hydrogen generation, storable solar energy can be used to combat the destructive and finite fossil fuel consumption of the world.

References

1. Eckenhoff, W., & Eisenberg, R. (2012). Molecular systems for light driven hydrogen production. *Dalton Trans.*, 41(42), 13004-13021.
2. Simmons, Berggren, Bacchi, Fontecave, & Artero. (2014). Mimicking hydrogenases: From biomimetics to artificial enzymes. *Coord. Chem. Rev.*, 270-271, 127-150.
3. Yu, Tianjun, Zeng, Yi, Chen, Jinping, Zhang, Xiaohui, Yang, Guoqiang and Li, Yi. (2014) Efficient photochemical production of hydrogen in aqueous solution by simply incorporating a water-insoluble hydrogenase mimic into a hydrogel. *J. Mat. Chem*. A, 2, 20500-20505.
4. Singleton, M., Crouthers, D., Duttweiler, R., Reibenspies, J., & Darensbourg, M. (2011). Sulfonated diiron complexes as water-soluble models of the Fe-Fe-hydrogenase enzyme active site. *Inorg. Chem.*, 50(11), 5015-26.
5. G. P. Connor, K. J. Mayer, C. S. Tribble, and W. R. McNamara. (2014). Hydrogen Evolution Catalyzed by an Iron Polypyridyl Complex in Aqueous Solutions. *Inorg. Chem.* **2014,** 53 (11), 5408-5410.
6. Hartley, C.L., DiRisio, Ryan J., Chang, T.C., Zhang, W., & Mcnamara, W. R. (2016). Electrocatalytic hydrogen evolution by an iron complex containing a nitro-functionalized polypyridyl ligand. *Polyhedron*, 114, 133-137.
7. Cavell, A. C.; Hartley, C. L.; Liu, D.; Tribble, C. S.; McNamara, W. R. (2015). Sulfinato Iron(III) Complex for Electrocatalytic Proton Reduction. *Inorg. Chem.* 54(7), 3325-3330.
8. Hartley, C., Dirisio, R., Screen, M., Mayer, K., & Mcnamara, W. (2016). Iron Polypyridyl Complexes for Photocatalytic Hydrogen Generation. *Inorg. Chem.*, 55(17), 8865-8870.
9. Mayilmurugan, R.; Visvaganesan, K.; Suresh, E.; Palaniandavar, M. *(*2009). Iron(III) Complexes of Tridentate 3N Ligands as Functional Models for Catechol Dioxygenases: The Role of Ligand N-alkyl Substitution and Solvent on Reaction Rate and Product Selectivity *Inorg. Chem.* 48, 8771-8783.
10. Viswanathan, R.; Palaniandava, M.; Blasubramanian, T.; Muthiah, P.T. *Inorg. Chem.* 1998, 37, 2943.
11. Thapper, A.; Behrens, A.; Fryxelius, J.; Johansson, M. H.; Prestopino, F.; Czaun, M.; Rehder, D.; Nordlander, E. (2005) Synthesis and characterization of molybdenum oxo complexes of two tripodal ligands: reactivity studies of a functional model for molybdenum oxotransferases. *Dalton Trans*. 3566-3571
12. Imbert, C.; Hratchian, H.P.; Lanznaster, M.; Heeg, M.J.; Hryhorczuk, L.M.; McGarvey, B.R.; Schlegel, H.B.; Verani, C.N. (2005). Influence of Ligand Rigidity and Ring Substitution on the Structural and Electronic Behavior of Trivalent Iron and Gallium Complexes with Asymmetric Tridentate Ligands. *Inorg. Chem.* 44, 7414-7422.
13. Lanznaster, M.; Neves, A.; Bortoluzzi, A.J.; Assumpcao, A.M.C.; Vencato, I.; Machado, S.P.; Drechsel, S.M. (2006) Electronic Effects of Electron-Donating and -Withdrawing Groups in Model Complexes for Iron-Tyrosine-Containing Metalloenzymes. *Inorg. Chem.* 45, 1005-1011.
14. Prier, C., Rankic, D., & Macmillan, D. (2013). Visible Light Photoredox Catalysis with Transition Metal Complexes: Applications in Organic Synthesis. *Chem. Rev., 113*(7), 5322-5363.
15. Roy, S., Bacchi, M., Berggren, G., & Artero, V. (2015). A Systematic Comparative Study of Hydrogen-Evolving Molecular Catalysts in Aqueous Solutions. *ChemSusChem, 8*(21),

3632-3638.

16. Wise, C., Liu, D., Mayer, K., Crossland, P., Hartley, C., & Mcnamara, W. (2015). A nickel complex of a conjugated bis-dithiocarbazate Schiff base for the photocatalytic production of hydrogen. *Dalton Trans., 44*(32), 14265-14271.

17. Han, Z., McNamara, W., Eum, M., Holland, P., & Eisenberg, R. (2012). A Nickel Thiolate Catalyst for the Long-Lived Photocatalytic Production of Hydrogen in a Noble-Metal-Free System. *Angew. Chem. Int. Ed.,* 51(7), 1667-1670.

18. Lazarides, T.; McCormick, T.; Du, P.; Luo, G.; Lindley, B.; Eisenberg, R. (2009). Making Hydrogen from Water Using a Homogeneous System Without Noble Metals. *J. Am. Chem. Soc*., 131, 9192-9194.

19. Hartley, C. (2016) Iron Complexes for Photocatalytic Hydrogen Generation. *Undergraduate Honors Theses*. Paper 909. http://publish.wm.edu/honorstheses/909

20. Streich, D., Astuti, Y., Orlandi, M., Schwartz, L., Lomoth, R., Hammarström, L., & Ott, S. (2010). High-Turnover Photochemical Hydrogen Production Catalyzed by a Model Complex of the [FeFe]-Hydrogenase Active Site. *Chem.–Eur. J.*, 16(1), 60-63.

21. Han, Z., Qiu, F., Eisenberg, R., Holland, P., & Krauss, T. (2012). Robust Photogeneration of H_2 in Water Using Semiconductor Nanocrystals and a Nickel Catalyst. *Science*, 338(6112), 1321-1324.
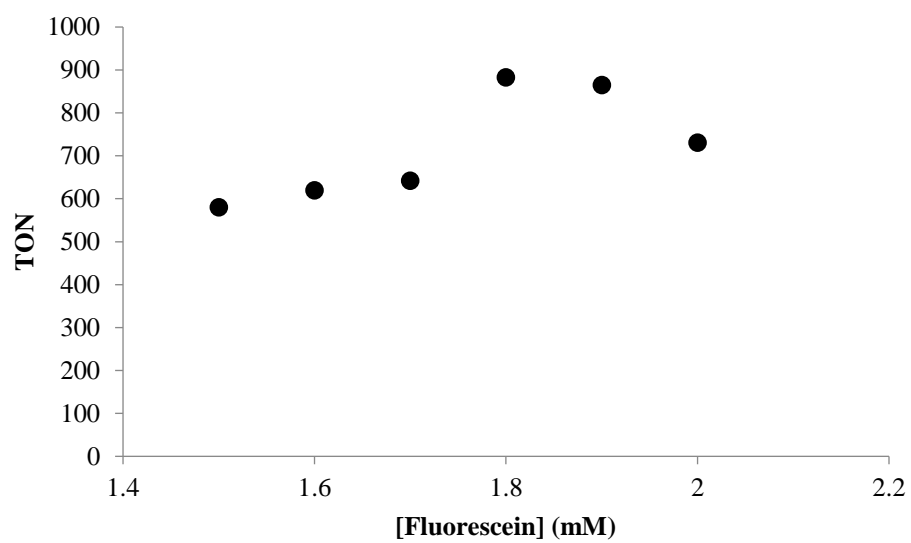
Appendix A

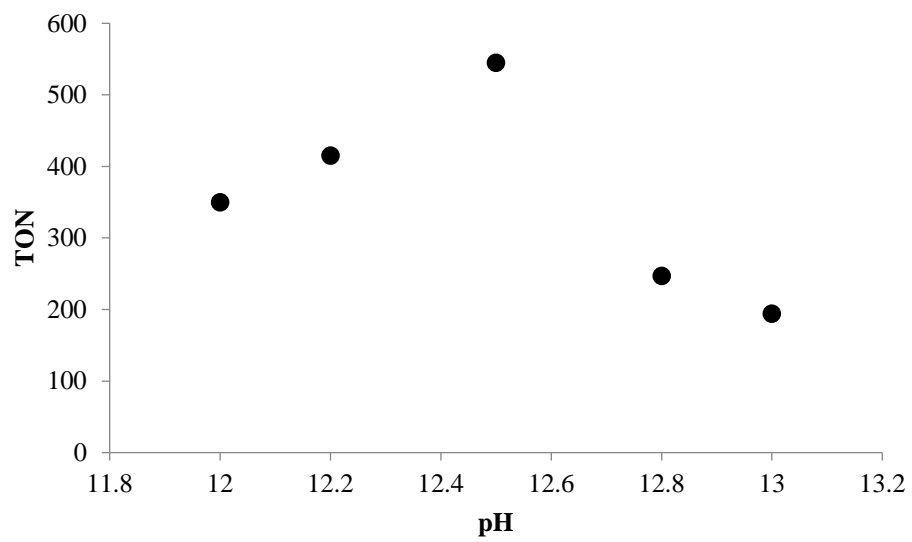**Figure A1**. Varying [fluorescein] and measuring subsequent TONs in a system with **2** after 12 hours of irradiation**.**

Figure A2. Varying pH and measuring subsequent TONs in a system with **2** after 12 hours of irradiation**.**
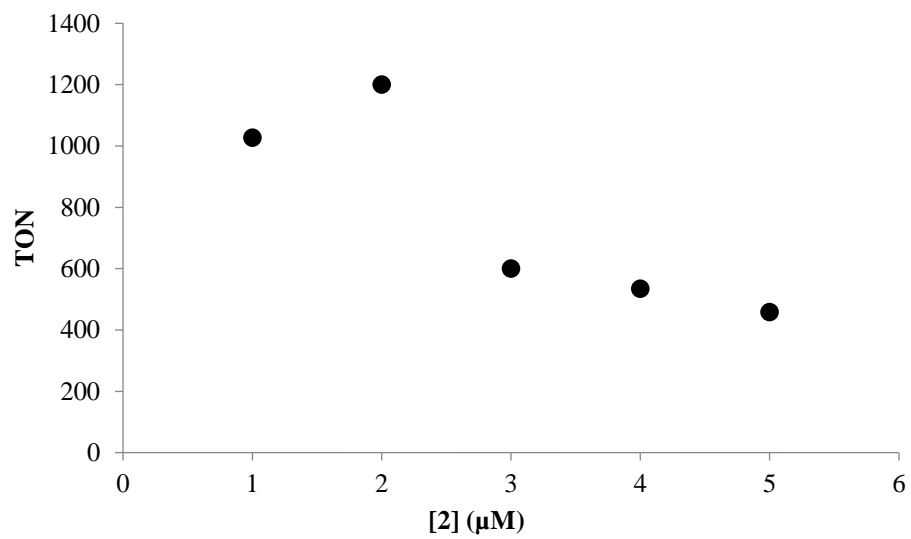
Figure A3. Varying [**2**] and measuring subsequent TONs in a system after 12 hours of irradiation.
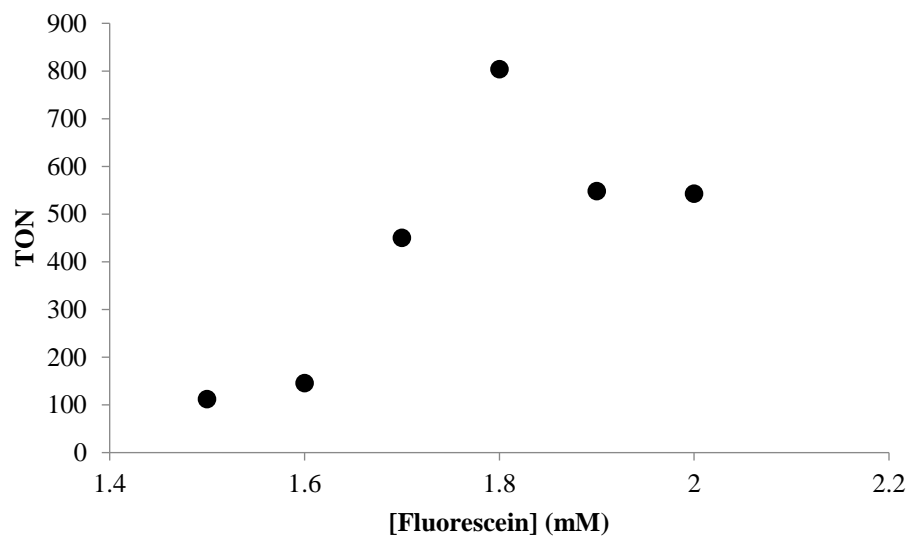
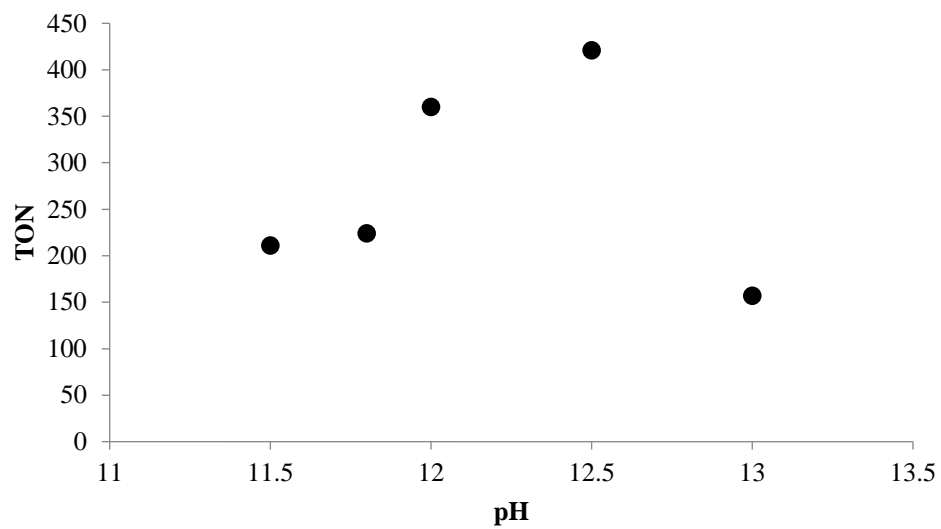**Figure A4** Varying [fluorescein] and measuring subsequent TONs in a system with **3** after 12 hours of irradiation**.**

Figure A5. Varying pH and measuring subsequent TONs in a system with **3** after 12 hours of irradiation.
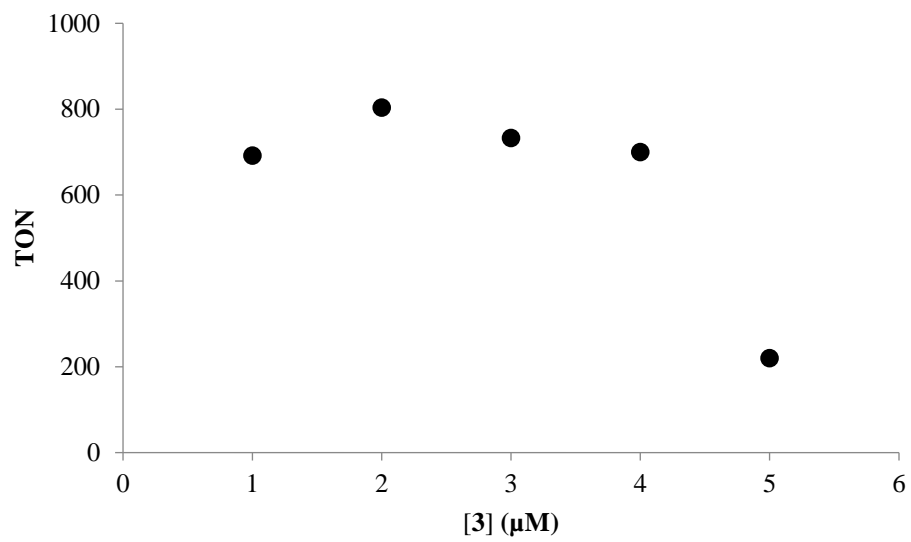
Figure A6 Varying [**3**] and measuring subsequent TONs in a system after 12 hours of irradiation.

Catalyst	Fluorescein/TEA TON	Eosin Y/TEOA TON	Eosin Y/TEA TON	Ru(bpy)$_3$$^{2+}$/Ascorbic Acid TON
1	1132	2	385	0
2	421	0	319	0
3	545	0	164	0

Table A1. Chromophore and Sacrificial Donor optimization studies. Fluorescein and TEA exhibited the highest amount of activity from each of the studies.

Quantum Yield Equations and Sample Calculation:
Quantum yield is calculated using the following equations[21]:

(A1)
$$P = \frac{c*h*n}{\lambda*t}$$

(A1.5)
$$\frac{n}{t} = \frac{P*\lambda}{c*h} \quad (n = \text{\# of photons})$$

(A2)
$$q_p = \frac{n}{t} = \frac{P*\lambda}{c*h}$$

(A3)
$$k = \frac{n}{t} \quad (n = \text{\# moles of hydrogen produced})$$

(A4)
$$q_p = \frac{P*\lambda}{c*h}$$

(A5)
$$\phi_{H_2} = \frac{2k}{q_p}$$

Where c is the speed of light (m/s), h is the Planck constant (m^2*kg/s), t is time (s), λ is wavelength (m), k is the amount of hydrogen produced over time (mols/s), and q$_p$ is photo flux (photons/s).

Sample calculation:

$$k = \frac{moles\ H_2\ Produced}{time}$$

$$k = \frac{6.32(10^{-6})}{86400s} = \frac{7.31(10^{-11})moles}{s}$$

$$P = Measured\ power - background\ measurements$$

$$P = 1.86(10^{-3})W - 910(10^{-6})W = 9.50(10^{-4})W$$

$$q_p = \frac{P*\lambda}{c*h} = \frac{9.50(10^{-4})W * 520 * 10^{-9}m}{3.00(10^8) * 6.626 * 10^{-34}} = 2.49(10^{15})s^{-1}$$

$$\frac{q_p}{mol} = \frac{2.49(10^{15})s^{-1}}{6.02(10^{23})\frac{photons}{mol}} = 4.14(10^{-9})\frac{mol}{s}$$

$$\Phi_{H_2} = \frac{2k}{q_p} = \frac{2 * 7.31(10^{-11})\frac{mol}{s}}{4.14(10^{-9})\frac{mol}{s}} * 100 = 3.5\%$$
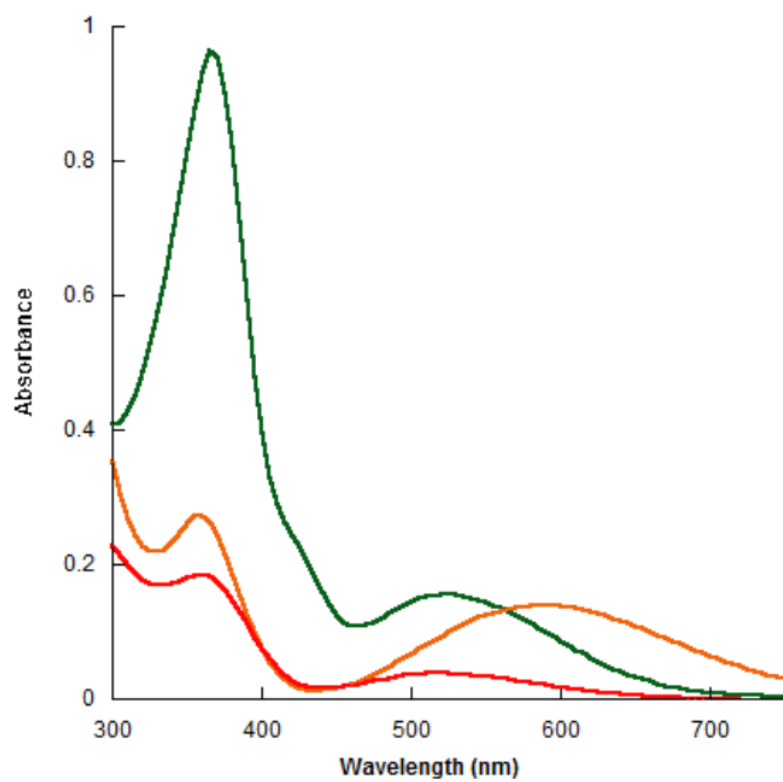
Figure A7. UV-Vis spectra of **1** (orange), **2** (green), and **3** (red).
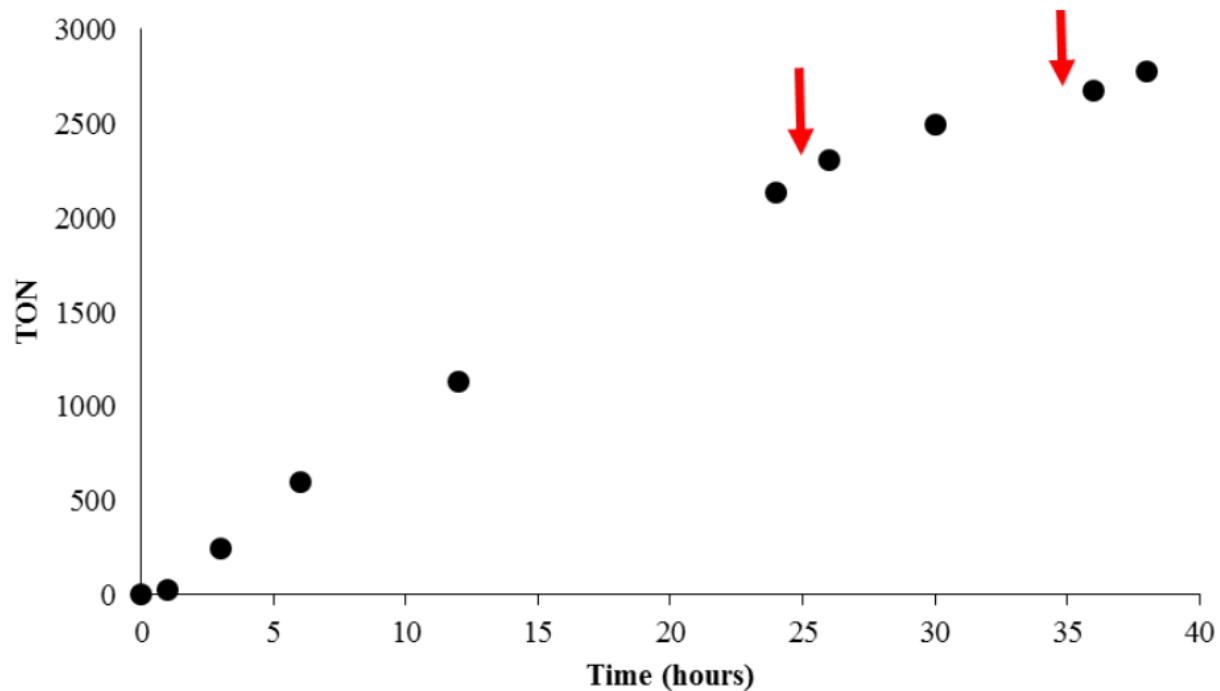
Fl Addition Experiments

Figure A8. Hydrogen generation over time study with 100 μl of 4.0 mM fluorescein additions at the 25th and 35th hour using optimal conditions for **1**. These additions showed a return to a linear increase in hydrogen generation, supporting the idea that fluorescein is decomposing rather than the catalysts in solution for up to 36 hours.

Chapter III. Cost-Effective Cobalt Complexes for Electrocatalytic Proton Reduction

Introduction

Cobalt is another transition metal that has been the subject of research in the pursuit of a catalyst for proton reduction. Cobalt, like iron, is a common, cost-effective metal. Using other cost-effective reagents in conjunction with a cobalt center could generate an extremely cost-effective complex. Cobalt complexes have been shown to be electrochemically[1] and photocatalytically[2] active for hydrogen generation, meaning that there is an opportunity to synthesize an extremely low cost, active, and efficient complex for proton reduction.

Recently, our group reported a pair of octahedral cobalt electrocatalysts for proton reduction.[3] One of the ligands was functionalized with two nitro electron-withdrawing groups to pull electron density away from the metal center, which allows for a more facile reduction of the metal center.[3]

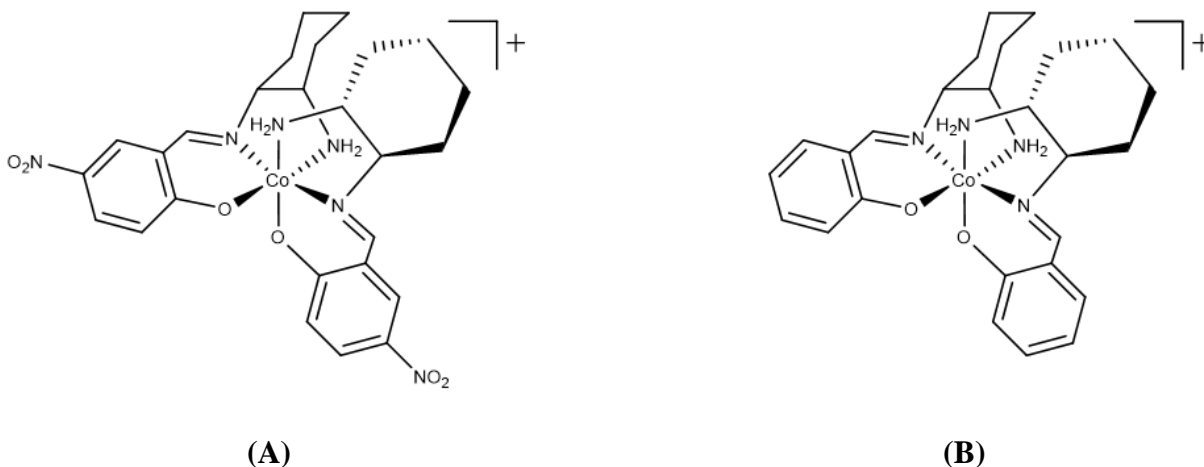(A)   (B)

Figure 3.1. Nitro-substituted Schiff base cobalt complex (left), and the non-substituted complex (right).

Upon electrochemical experiments, only **A** exhibited electrocatalytic activity for proton reduction.[3] Interestingly, without the electron withdrawing group, **B** did not exhibit any

electrocatalytic activity. For **B**, electrochemical experiments only showed the background

reduction of acid in solution.[3] Furthermore, **A** and **B** were both stereochemically active, giving

multiple isomers through their syntheses.[3] It was of great interest to explore refining **A** to

improve its catalytic activity and its efficiency, as well as eliminate the possibility of a

stereochemically mixed product. To this end, two derivatives were synthesized due to their easy

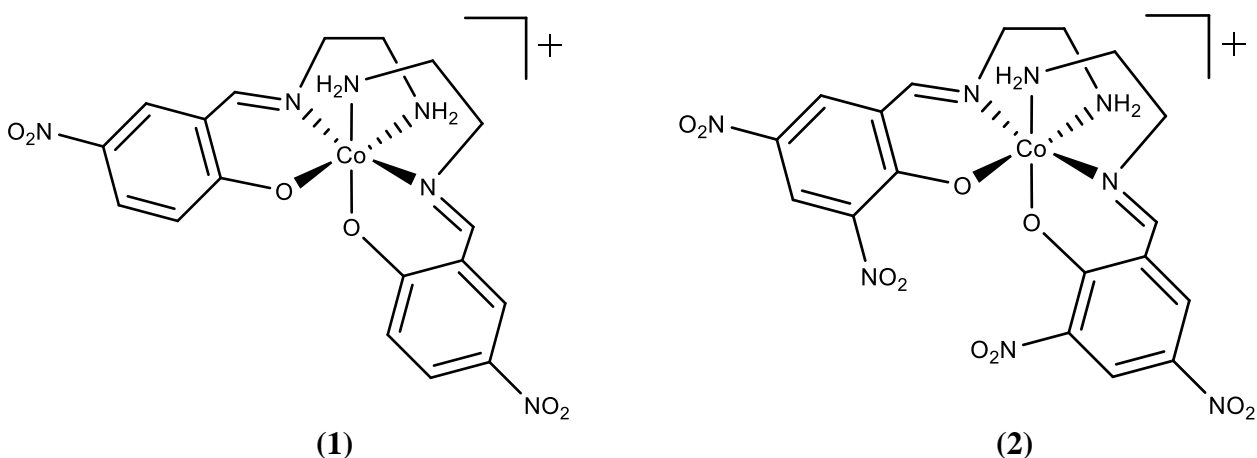and isomerically pure synthesis and their cost-effectiveness.

Figure 3.2. A dinitro functionalized Schiff-base cobalt complex (**1**) and a tetranitro substituted Schiff-base cobalt complex (**2**).

1 and **2** are both functionalized with nitro groups to pull electron density away from the

metal center, hypothetically making reduction of the metal center easier. **1** is functionalized with

2 nitro groups while **2** is functionalized with 4. The diaminocyclohexyl group was replaced with

cost-effective ethylene diamine, which additionally lowers the cost of the complex. The ethylene

diamine also eliminates the chance for isomers, leading to a stereochemically pure product. With

the variation of electron withdrawing groups, the two catalysts can be compared with respect to

overpotential and catalytic rate.

The overpotential and the catalytic rates of **1** and **2** were measured using cyclic

voltammetry. As mentioned before, current response is measured by introducing a potential into

a solution with the catalyst of interest. Without acid present, the catalyst should undergo a reduction event when the potential is scanned cathodically, and an oxidation when the potential is scanned back anodically. This takes the form of a reversible redox couple as seen in Figure 3.3 in black. Once acid is added to the solution, an irreversible catalytic reduction event is observed when the potential is scanned cathodically, which corresponds to the reduction of protons by the catalyst to hydrogen.
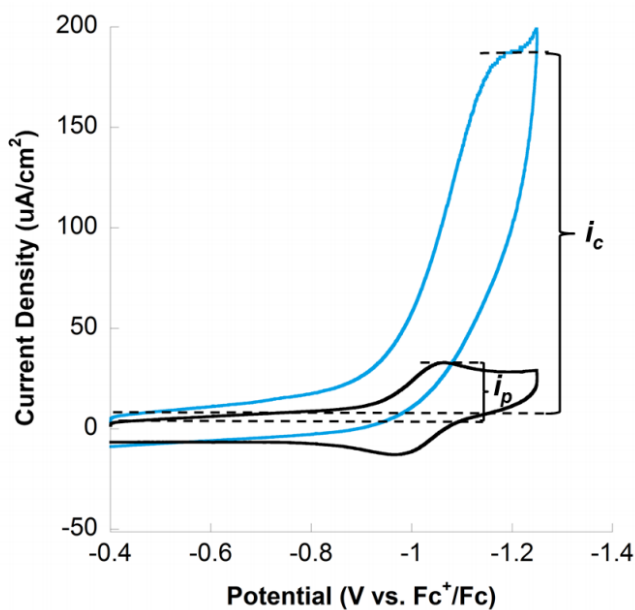

Figure 3.3. Determination of i_c/i_p.[3] The current response with acid (blue) is divided by the current response without acid (black).[3]

Information on catalytic activity and efficiency can be then calculated using these current responses. To quantify the activity of the complex, a metric called i_c/i_p is used. The derivation of i_c/i_p is as follows:

Current response in the presence of acid is written:[4]

$$i = \frac{nFAC_p^0\sqrt{Dk_{obs}}}{1 + e^{\left[\frac{F}{Rt}(E-Eredox)\right]}}$$

Current response without acid is written:[4]

$$i_p = 0.4463FAC_p^0\sqrt{\frac{F\nu D}{RT}}$$

Where i is current, i_p is the peak current of the reduction event of the redox couple, n is the

number of electrons involved in the proton reduction process, n is the number of electrons

involved in the hydrogen evolution (2 electronics are needed), F is the Faraday Constant, A is

the surface area of the electrode, C_p^0 is the bulk concentration of acid, k_{obs} is the rate constant (s⁻

¹), R is the gas constant, T is temperature, E is the varying potential as the CV scans, and E_{redox} is

the potential at which the reduction/oxidation response occurs without acid.[4] Once the difference

between the applied potential and the redox potential is greater than 100mV,[4] which occurs

during or before the irreversible reduction event, the denominator of the above equation becomes

insignificant, and the ratio of the two equations is written as:

$$i_c = nFAC_p^0\sqrt{Dk_{obs}}$$

$$\frac{i_c}{i_p} = \frac{n}{0.4463}\sqrt{\frac{RT}{F\nu}k_{obs}}$$

i_c is the current at the peak of the catalytic plateau typically formed under ideal

conditions.[4] From this equation, the universal k_{obs} can be calculated. As a rate constant, k_{obs} can

be used to calculate TOF. As mentioned before, TOF is a universal metric to compare the

electrocatalytic activity for homogeneous catalysts.

In addition to measuring catalytic activity, it is important to assess the efficiency of the

catalysts as well. The additional energy needed for proton reduction to occur beyond its

thermodynamic potential is important to the overall system. With a high amount of additional

energy, the catalyst is barely reducing the activation energy required of the reaction. However,

with a low barrier, less energy needs to be implemented in the system for proton reduction to

occur. The quantification of this additional energy takes the form of overpotential.

Overpotential can be measured from CVs, as seen in the Figure 3.4. Overpotential is measured by taking the difference between the half wave potential of the catalytic wave and a reference potential. This reference potential is a literature value, reflecting the reduction potential of an acid in a particular solvent. However, due to the non-ideal behavior of catalytic waves, it is difficult to observe an accurate half wave potential, and therefore it is difficult to calculate overpotential accurately.[4] In addition, it is difficult to calculate the reduction potential of various acids in organic solutions due to many factors, including homoconjugation and measuring pKa values.[4] As such, the values of the reduction potentials of acids in particular solvents are controversial.[4]
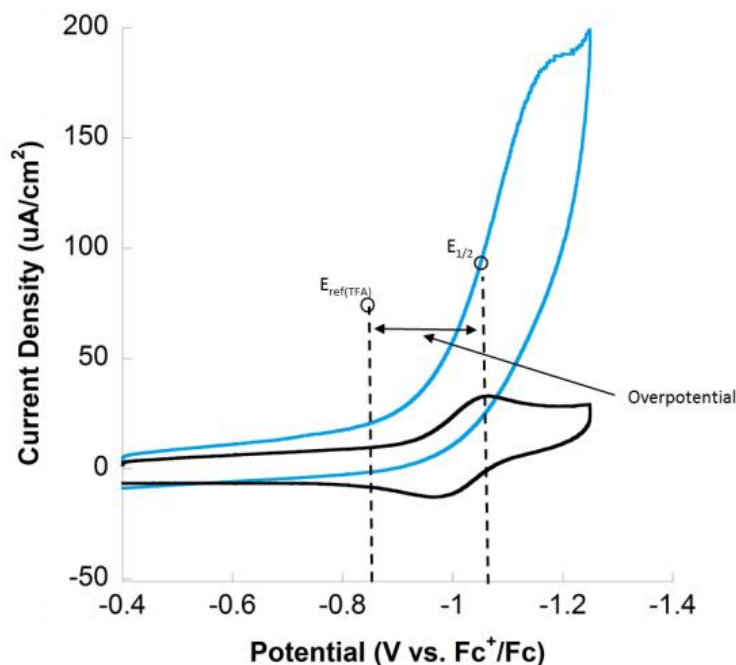

Figure 3.4. Determination of overpotential by subtracting the catalytic half wave potential ($E_{1/2}$) from an acid-solvent specific reference value (E_{ref}) from literature.[3]

For the catalysts presented by McNamara and coworkers, a slightly modified version of

the i_c/i_p equation is needed:[3]

$$\frac{i_c}{i_p} = \frac{n}{0.4463}\sqrt{\frac{RT}{Fv}} k_{obs} * [H^+]^2$$

This is because the catalytic response of the cobalt catalyst is second order with respect to acid, rather than treating the hydrogen generation process as pseudo-first order.[3,5] In order to calculate k_{obs}, a new technique is needed. When plotting i_c/i_p vs. [H+], a slope can be calculated. From this, plotting the slope of i_c/i_p vs. the inverse square root of the different scan rate experiments yield an m value. From this m value, k_{obs} can be calculated:

$$m = \frac{\left(\frac{i_c}{i_p}\right) * \sqrt{v}}{[H^+]^2}$$

Rearranging the equation:

$$\frac{\left(\frac{i_c}{i_p}\right) * \sqrt{v}}{[H^+]^2} = \frac{n}{0.4463} * \sqrt{\frac{RTk_{obs}}{F}}$$

$$k_{obs} = \frac{F}{RT} * \left(\frac{0.4463m}{n}\right)^2 \ in \ (M^{-1})^2 * s^{-1}$$

From that value, a TOF can be calculated by multiplying by the bulk concentration of the acid present in the cell to leave the value in s^{-1}.

McNamara and coworkers reported a TOF of 420 s^{-1}, an i_c/i_p of 5.16, and an overpotential value of 350 mV for the nitro-substituted cobalt complex.[3] This complex was shown to be an active electrocatalyst for proton reduction.[3] However, the analytic techniques used to report these numbers do not take into account the issues of the non-ideal catalytic response, and there is room for improvement on the cost and the efficiency of these complexes.

Recently, however, there have been new approaches to report both the kinetics and

theoretical maximum activity of molecular electrocatalysts. Foot-of-the-Wave Analysis (FOWA) was developed by Savéant et. al. to correct for the non-ideal character of many CVs.[6] Ideally, an irreversible reduction peak would be S-shaped, as seen in Zone KS in Figure 3.5 below.[4]

$$(1) \; \lambda = \frac{RT}{F} \left(\frac{k_e C_p^0}{v} \right)$$

$$(2) \quad \gamma = C_a^0 / C_p^0$$

λ, represented in Equation (1), is a kinetic parameter that addresses the kinetics of electron transfer from the catalyst to a proton, where R is the universal gas constant, T is temperature, F is the Faraday constant, k_e is the rate constant of the outer sphere electron transfer from the catalyst to the hydrogen, C_p^0 is the bulk concentration of catalyst in solution, and v is the scan rate.[4] γ, represented in Equation (2) is the excess factor in solution, which is the ratio of the concentration of protons to catalyst present.[4]
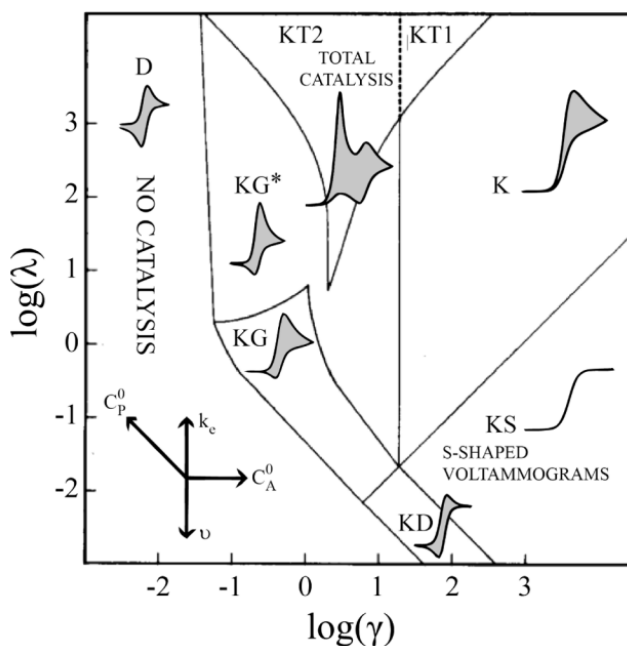

Figure 3.5. CVs exhibiting various types of ideal and non-ideal behavior. Zone KS CVs are ideal for catalytic response currents, while all others, including Zone K, are non-ideal. Courtesy of Dempsey and coworkers.[4]

This S shape implies that there are no side reactions or phenomena disturbing the current

response while the potential was applied.[6] At high concentrations of protons and high rates of electron transfer, Zone K behavior is shown. Observation of our CVs in Appendix B shows that our complexes exhibit Zone K behavior. Proton consumption is one of the biggest factors for the non-ideal character of Zone K behavior, because the catalytic reaction is limited by proton consumption and the need for new protons to flow into the reaction space.[4] In addition to proton consumption, other side phenomena, like catalyst decomposition, can also be a contributing factor to non-ideal behavior.[4]
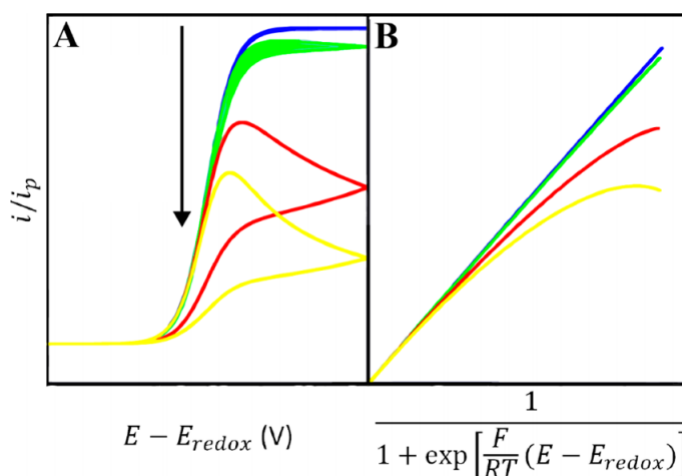

Figure 3.6. CVs and their Corresponding FOWA plots, from ideal (blue) to non-ideal (yellow).[4]

To correct for the non-ideal character of the waves, Savéant and coworkers show that the 'foot' of non-ideal catalytic waves resemble the theoretical ideal[7]. Using the same initial equation:[4]

$$i = \frac{2FAC_p^0\sqrt{Dk_{obs}}}{1 + e^{\left[\frac{F}{Rt}(E-E_{redox})\right]}}$$

Since the applied potential term $(E - E_{redox})$ is in relation to the redox couple of the complex of interest, the reference through which the current is measured (such as Fc[+]/Fc, SHE, or SCE) is

irrelevant. Additionally, the Randles-Sevcik equation describes peak current of a reversible

catalytic wave while incorporating parameters such as scan rate and temperature:[4]

$$i_p = 0.4463 FAC_p^0 \sqrt{\frac{FvD}{RT}}$$

Combining the two equations:

$$\frac{i}{i_p} = \frac{2\sqrt{\frac{RT}{Fv}}\sqrt{k_{obs}}}{0.4463} * \frac{1}{1 + e^{\left[\frac{F}{Rt}(E-Eredox)\right]}}$$

i/i_p is then plotted versus $\frac{1}{1+e^{\left[\frac{F}{Rt}(E-Eredox)\right]}}$. The rate gathered from the FOWA equation

describes the first chemical step of the reaction, typically hydride formation.[7] The linear portion

of this wave corresponds to the ideal portion the catalytic wave.[4] See Figure 3.10 to observe the

portion of the wave that corresponds to the linear FOWA region. Taking the slope of this

regions gives:

$$m = \frac{2\sqrt{\frac{RT}{Fv}}\sqrt{k_{obs}}}{0.4463}$$

$$k_{obs} = \frac{(m^2)(0.4463)^2 Fv}{4RT}$$

From this slope, a k_{obs} rate constant can then be extracted in the units s^{-1}. From this rate constant,

a catalytic rate constant of the first chemical step can be calculated by dividing the rate constant

by the bulk acid concentration in solution, which is in units s^{-1}M^{-1}:[7]

$$k_1 = \frac{k_{obs}}{[H^+]}$$

This rate constant, if it is determined to be the rate determining step (RDS), can be used to

ideally describe the catalytic activity of complexes for hydrogen generation. This k_1 is then

called k_{cat}. However, the first chemical step of the reaction is not necessarily rate-determining.

It is generally assumed that the electrical steps of a proton-coupled electron transfer process are not rate limiting.[7] However, the kinetics surrounding the second chemical step of the catalytic mechanism are not known. There have been experiments performed in the literature to determine if k_1 is the RDS of a cobalt catalyst,[7] which will be discussed in a later section. Nevertheless, with such a catalytic rate constant, the catalyst can be benchmarked and compared to other catalysts, all of which use the theoretical ideal portion of their waves.

The FOWA technique does not, however, take into account the efficiency of the catalyst. Therefore, it is of interest to explore the TOF-overpotential relationship. Specifically, a benchmark that can be used to compare catalysts is the catalyst's theoretical catalytic rate at 0 overpotential. This will be able to show the theoretical ideal behavior of the catalyst with respect to activity and efficiency. To describe the theoretical catalytic rate of the complex at 0 overpotential (η), Tafel Plots are used.[4] The equations to determine Tafel plots are shown below:[7,8]

$$\textbf{(3)} \quad TOF = \frac{TOF_{max}}{1+e^{\left(\frac{F}{RT}\right)(E-E_{Redox})}}$$

$$\textbf{(4)} \quad \eta = E^0_{H+/H_2} - E$$

$$\textbf{(5)} \quad TOF = \frac{TOF_{max}}{1+e^{\left(\frac{F}{RT}\right)\left(E^0_{H+/H_2}-\eta-E_{Redox}\right)}}$$

Generally speaking, TOF can be expressed using Equation (3). TOF_{max} is equal to the observed rate constant from the FOWA technique, in s^{-1} at a conventional 1 M acid.[8] From this equation, overpotential (η) can be incorporated into Equation (1), and TOF can be written has Equation (3). Overpotential is represented as the reduction potential of a particular acid in a solvent subtracted by the applied potential. Equation (3), however, is still reduced to Equation (1) if η is replaced by the right side of Equation (2). Nevertheless, this means that TOF can be

plotted versus η. This is typically done in a logarithmic manner. The result shows a leveling of catalytic activity at a particular overpotential, and a TOF at 0 overpotential.
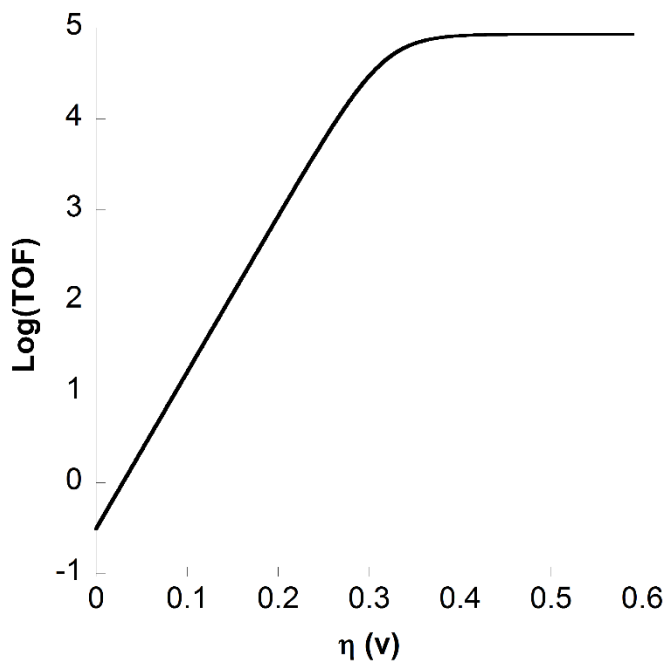

Figure 3.7. Tafel plot of **1** at ν = 1 v/s.

In this chapter, a novel pair of cobalt complexes are reported due to their low cost and easy synthesis. The synthesis and characterization of these novel cobalt complexes will be reported. In addition, the electrocatalytic activity of both complexes are measured using the new techniques of FOWA and Tafel Plots to more ideally describe their activity and efficiency, as well as moving them in line with the current standards of catalyst comparison.

Experimental

Materials and Methods

Experiments were performed under an atmosphere of argon unless stated otherwise. Chemicals being purchased from places.

Instrumentation

^{1}H and ^{13}C Spectra Agilent 400MR DD2 Spectrometer operating in the pulse Fourier transform mode, and chemical shifts are referenced to residual solvent. Mass spectrometry was performed using positive-ion mode electrospray ionization on an Apollo II ion source on a Bruker 12.0 Tesla APEX-Qe FTICR-MS.

X-Ray Diffractometry

Single Crystal X-Ray Diffractometry was performed by William W. Brennessel at the X-Ray Crystallographic Facility at the University of Rochester. Analysis was performed using a Bruker SMART APEX II CCD platform diffractometer.

(1). A crystal (0.48 x 0.20 x 0.12 mm^3) was placed onto the tip of a thin glass optical fiber and mounted on a Bruker SMART APEX II CCD platform diffractometer for a data collection at 100.0(5) K.[9] A preliminary set of cell constants and an orientation matrix were calculated from reflections harvested from three orthogonal wedges of reciprocal space. The full data collection was carried out using MoKα radiation (graphite monochromator) with a frame time of 10 seconds and a detector distance of 3.99 cm. A randomly oriented region of reciprocal space was surveyed: twelve major sections of frames were collected with 0.50º steps in ω at twelve different ϕ settings and a detector position of -38º in 2θ. The intensity data were corrected for absorption.[10] Final cell

constants were calculated from the xyz centroids of 3983 strong reflections from the actual data collection after integration.[11]

(**2**). A crystal (0.48 x 0.20 x 0.12 mm^3) was placed onto the tip of a thin glass optical fiber and mounted on a Bruker SMART APEX II CCD platform diffractometer for a data collection at 100.0(5) K.[9] A preliminary set of cell constants and an orientation matrix were calculated from reflections harvested from three orthogonal wedges of reciprocal space. The full data collection was carried out using MoKα radiation (graphite monochromator) with a frame time of 10 seconds and a detector distance of 3.98 cm. A randomly oriented region of reciprocal space was surveyed: seven major sections of frames were collected with 0.50º steps in ω at seven different ϕ settings and a detector position of -38º in 2θ. The intensity data were corrected for absorption.[10] Final cell constants were calculated from the xyz centroids of 3787 strong reflections from the actual data collection after integration.[11]

Synthesis
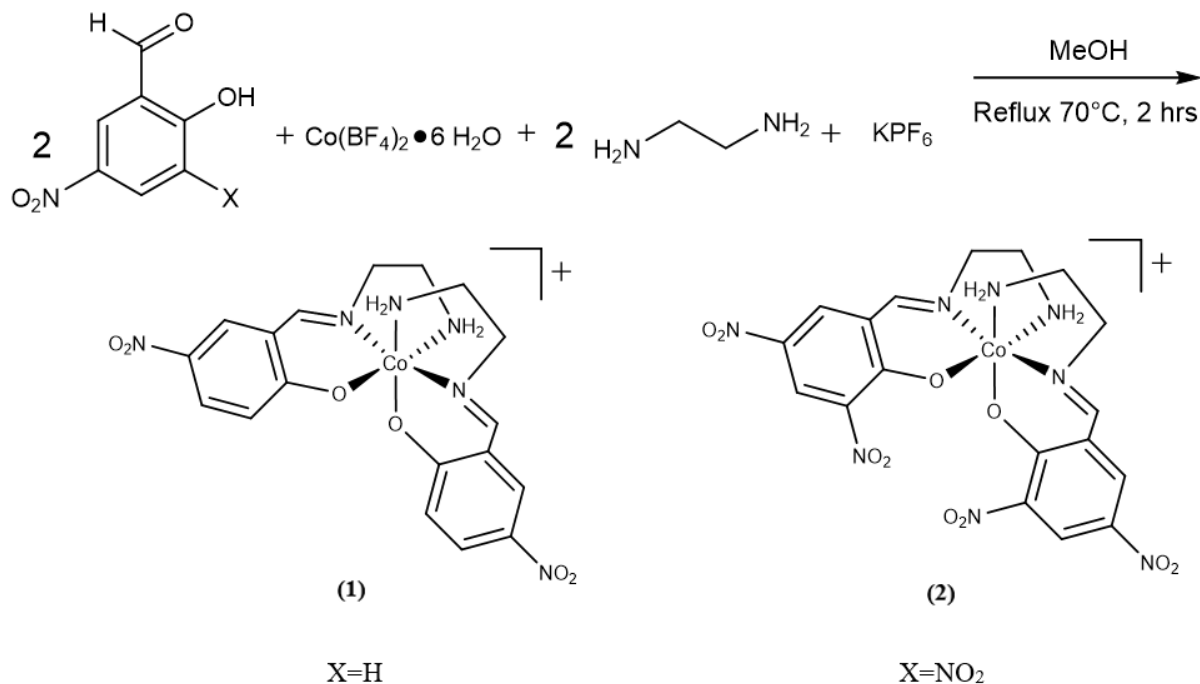
Scheme 3.1. Synthesis Scheme of **1** and **2**.

1. 1 was synthesized in air. 1.5 mmol of 2-hydroxy-5-nitrobenzaldehyde and 0.75 mmol of

Cobalt(II)tetrafluoroborate were dissolved in methanol. 1 mL ethylene diamine and 0.75 mmol

potassium hexafluorophosphate were both added into solution. This solution was heated to 70°C

for two hours After returning to room temperature, the solution was filtered and the solvent

evaporated via rotovap. A minimal amount of methanol was used to dissolve the remaining

solid. This was then filtered, and brought to concentration for crystallization by slow diffusion.

The methanol solution was layered on top of toluene. After approximately 48 hours, crystals

were harvested. (85% Yield).). MS: m/z expected = 475.077084; m/z found = 475.07690. ^{1}H

NMR (CDCl$_3$) δ: 4.08 (2 H, m); 4.23 (2H, m); 4.51 (4H, m); 6.66 (2H, d); 7.89 (2H, dd); 8.52

(2H, d); 8.82 (2H, s). ^{13}C NMR (CDCl$_3$) δ: 42.2, 62.2, 119.6, 122.8, 128.6, 132.5, 135.7, 167.0,

170.8.

2. 2 was synthesized in air. 1.5 mmol of 2-hydroxy-5-nitrobenzaldehyde and 0.75 mmol of

Cobalt(II)tetrafluoroborate hexahydrate were dissolved in methanol. 0.1 mL ethylene diamine

was added to solution. This solution was heated to 70°C for two hours. After returning to room

temperature, the solution was filtered and the solvent evaporated via rotovap. A minimal amount

of methanol was used to dissolve the remaining solid. This was then filtered, and brought to

concentration for crystallization by slow diffusion. The methanol solution was layered on top of

toluene. After approximately 48 hours, crystals were harvested. (56% Yield). MS: m/z

expected = 565.047240; m/z found = 565.046860. ^{1}H NMR (CDCl$_3$) δ: 4.17 (2 H, m); 4.32 (2H,

m); 4.96 (4H, s); 8.57 (2H, d); 8.81 (2H, d); 9.01 (2H, s). ^{13}C NMR (CDCl$_3$) δ: 21.9, 42.4, 125.1,

125.9, 133.9, 134.9, 142.8, 162.0, 166.7.

Electrochemistry Experiments

Cyclic Voltammetry (CV)

Cyclic voltammetry experiments were carried out using a CH Instruments 620D potentiostat.

The experiments used a three-electrode setup, with a standard calomel electrode. Electrodes were

polished using an alumina paste and washed with CH$_3$CN.

Acid Addition Study

Initially, in an electrochemical cell, 0.1 M TBAPF$_6$ was added to 5.0 mL of CH$_3$CN. The

solution was degassed using argon for 12 minutes. After, 0.2-0.5 mg of **1** or **2** were added to the

solution. A base scan was performed with no acid added. After, incremental additions, 35 μL,

70 μL, 105 μL, 140 μL additions for **1** at ν = 1 V/s and ν = 0.6 V/s, and 40, 80, 110, 140 uL

additions at ν = 0.2 V/s, were added. For **2**, 10 μL, 20 μL, 30 μL, 40 μL of 0.11 M trifluoroacetic

acid (TFA) were added.

Controlled Potential Coulometry (CPC)

CPC experiments were performed in a 4-neck round-bottom flask. **1** or **2** (0.5 mg) was added to 50 mL of 0.1 M TBAPF6 solution in CH_3CN. Two vitreous carbon electrodes and one silver wire reference electrode were inserted into the flask. The electrodes were submerged in solution and separated by VYCOR frits. The solution was degassed with argon, and TFA was added to a 65 mM concentration. The CPC was run at -1.2 V vs. Fc+/Fc for **1** and -1.0 vs. Fc+/Fc for **2** for 1800s, with a faradaic yield of 98%. No hydrogen was observed in the absence of catalyst.

Background Reduction of Trifluoroacetic Acid

In an electrochemical cell, 0.1 M $TBAPF_6$ was added to 5.0 mL of CH_3CN. The solution was degassed with argon for 12 minutes. A base scan was made prior to the addition of TFA, and then scans were taken after the addition of 13.2 mM TFA.

Dip Test for Homogeneity

In an electrochemical cell, 0.1 M $TBAPF_6$ was added to 5.0 mL of CH_3CN. 8.8 mM of TFA was also added along with **1** or **2**. A scan was taken, and the electrodes were removed from the cell. Without polishing, the electrodes were then placed in an electrochemical cell with 0.1 M $TBAPF_6$ and 5.0 mL of CH_3CN. Another scan was then taken.

Results and Discussion

The synthesis of **1** and **2** were both carried out in air. The 'one pot' reaction is a simple condensation reaction in one reaction vessel, and the reaction mixture is refluxed for only two hours. Upon characterization, the structures of **1** and **2** were as hypothesized. ^{13}C NMRs were taken and shown to match up with the theoretical peaks, and the molecular weight was confirmed by mass spectrometry. Through X-ray spectroscopy it was shown that both complexes exhibit octahedral geometry.
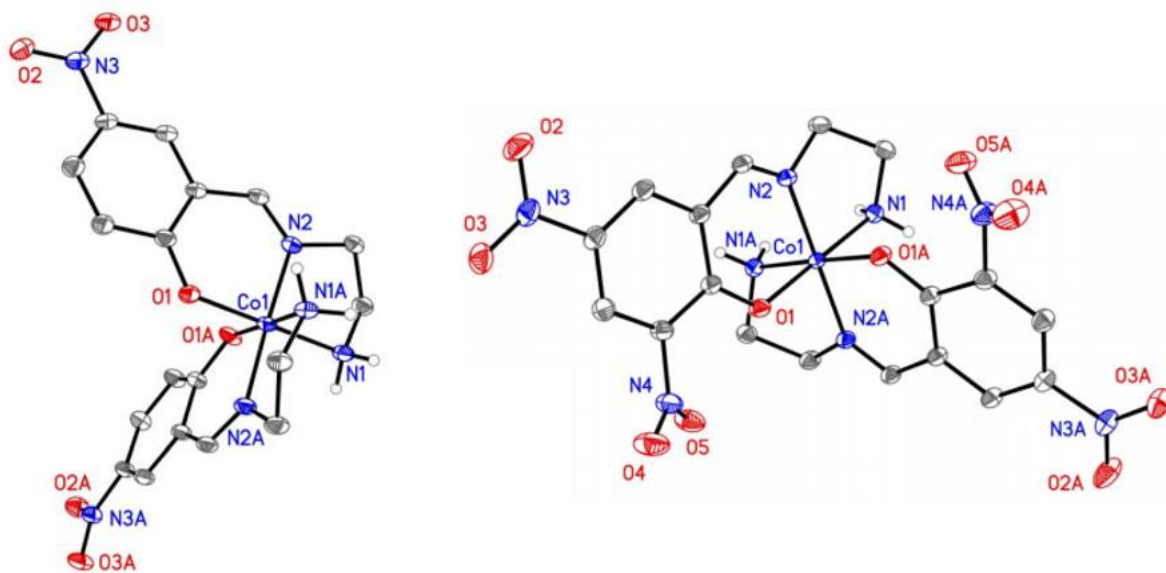
Figure 3.8. ORTEPs from X-Ray Crystallography of **1** (left) and **2** (right).

Bond Lengths (Å) for **1**		Bond Lengths (Å) for 2	
Co1-O(1A)	1.8940(9)	Co1-O(1A)	1.8958(9)
Co1-O(1)	1.8940(9)	Co1-O(1)	1.8959(9)
Co1-N(2)	1.9024(10)	Co1-N(2A)	1.9029(10)
Co1-N(2A)	1.9025(10)	Co1-N(2)	1.9029(10)
Co1-N(1)	1.9600(11)	Co1-N(1)	1.9540(10)
Co1-N(1A)	1.9600(11)	Co1-N(1A)	1.9541(10)
N(2)-C(3)	1.2837(15)	N(2)-C(3)	1.2818(15)

Bond Angles (º) for **1**		Bond Angles (º) for **2**	
O(1A)-Co1-O(1)	91.20(6)	O(1A) -Co1-O(1)	89.61(6)
O(1A) -Co1-N(2)	87.49(4)	O(1A) -Co1-N(2A)	94.05(4)
O(1)-Co1-N(2)	94.35(4)	O(1)-Co1-N(2A)	87.24(4)
O(1A) -Co1-N(2A)	94.35(4)	O(1A)-Co1-N(2)	87.24(4)
O(1)-Co1-N(2A)	87.49(4)	O(1)-Co1-N(2)	94.05(4)
N(2)-Co1-N(2A)	177.37(6)	N(2A) -Co1-N(2)	178.18(6)
O(1A) -Co1-N(1)	87.51(4)	O(1A)-Co1-N(1)	88.08(4)
O(1)-Co1-N(1)	178.66(4)	O(1)-Co1-N(1)	177.62(4)
N(2)-Co1-N(1)	85.27(4)	N(2A)-Co1-N(1)	93.52(4)
N(2A) -Co1-N(1)	92.93(4)	N(2)-Co1-N(1)	85.24(4)
O(1A) -Co1-N(1A)	178.67(4)	O(1A)-Co1-N(1A)	177.62(4)
O(1)-Co1-N(1A)	87.51(4)	O(1)-Co1-N(1A)	88.09(4)
N(2)-Co1-N(1A)	92.93(4)	N(2A) -Co1-N(1A)	85.25(4)
N(2A) -Co1-N(1A)	85.27(4)	N(2)-Co1-N(1A)	93.52(4)
N(1)-Co1-N(1A)	93.79(6)	N(1)-Co1-N(1A)	94.23(6)

Table 3.1. Selected bond lengths [Å] and angles [°] of **1** and **2**.

After successful characterization of **1** and **2**, the next step was to measure the

electrocatalytic activity and efficiency of the complexes through cyclic voltammetry. Using

crystals from the X-Ray crystallography experiments, CVs were taken of each complex at

different scan rates. Acid addition experiments showed a linear increase in current with respect

to concentration of TFA added, which indicates a second order dependence on H^+.[3] CVs of **1**

displayed a linear increase of current response up to 3.08 mM of acid, while **2** had a linear

increase to 0.88 mM acid (See Appendix B). **1** showed a redox potential of -0.938 V vs. Fc^+/Fc,

while **2** at -0.729 V vs. Fc^+/Fc, indicating **1** and **2** will both have lower overpotentials than **A**.

The redox potential of both complexes in the absence of acid was roughly equivalent to the half

wave potential of the catalytic current response, within 60 mV. This is useful for FOWA

calculations, as it is one of the qualifications to use relatively straightforward FOWA equations.

From these data, mechanistic insights can be made about the complex. The redox current

response disappears upon addition of acid. This indicates that the catalyst is oxidized through its

catalytic process rather than the introduction of the anodic potential.[4] It is hypothesized that **1**

and **2** most likely follow an EECC or ECEC mechanism. EC pathways are defined through the

different steps of proton-coupled electron transfer. The E stands for an electrical step of the

reaction, like a reduction, and the C stands for a chemical step, like the bonding of a hydride.[7]

FOWA was performed on both **1** and **2**. Theoretically, a perfect, S-shaped CV would be

a straight line on this plot. So, the small, linear portions gathered from CVs of **1** and **2** can be

considered the ideal portions of the wave. In Figure 3.10, a linear portion of the FOWA plot is

shown and its corresponding CV.

However, choice of where the 'foot' of the wave begins and ends is not explicitly defined

in literature. For the purposes of **1** and **2**, the current response leading up to the 'foot' of the

wave is not to be included in the analysis, as it is not a completely flat line, and the 'foot' of the wave portion taken ends where the FOWA plot starts to deviate significantly from linearity.
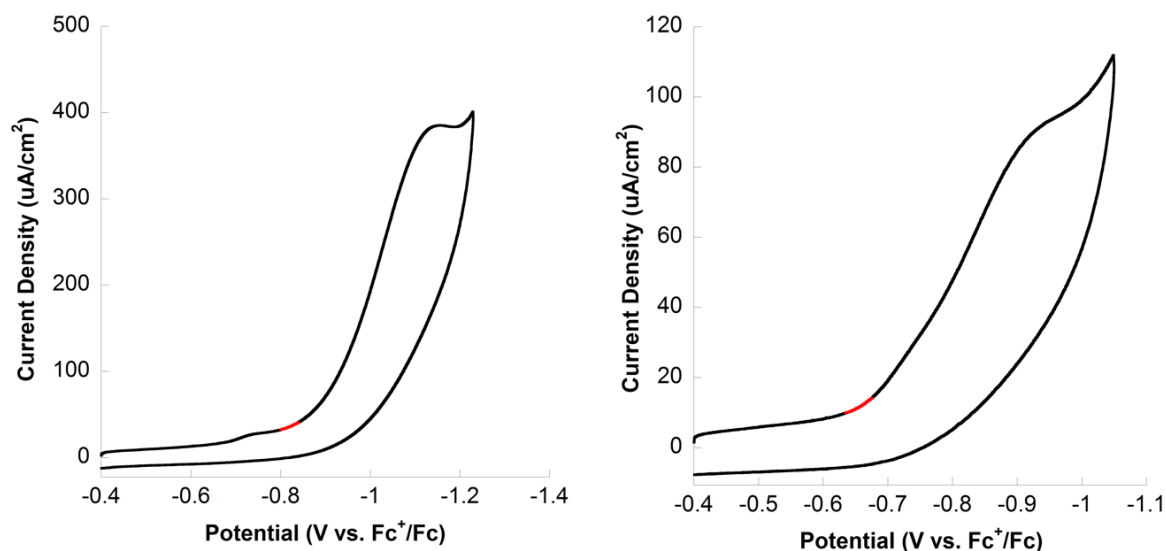

Figure 3.9. Portion of the wave taken for FOWA in red for **1** (Left) and **2** (Right).

From this portion of the wave, a rate constant k_{obs} is can theoretically-determined for each complex based on its ideal behavior. For an ECEC or EECC mechanism, it is important to note that $k_{obs} = k_1 * C_a^0$, where k_1 is the first chemical step in the mechanism.[7] It cannot be assumed that k_1 is the rate determining step for this reaction, and therefore it cannot be stated that k_1 is the rate-determining step (RDS) of the catalytic proton reduction mechanism. It is assumed that the electrical steps are not the hindering factors in the reaction.[7] However, to investigate if the first chemical step is rate determining, rather than the second chemical step, a literature procedure can be used.[7] In this procedure, it is useful to use the traditional method for determining catalytic activity using equation:[7]

$$\frac{i_c}{i_p} = \frac{n}{0.4463}\sqrt{\frac{RTk_1[H^+]}{Fv}}$$

To test whether k_1 or k_2 (the second chemical step) is the rate determining step, i_c/i_p

73

values are back calculated from k_1. To do this, k_1 can be substituted in easily, as it is the result of FOWA calculations. Even though k_2 was not measured, it can be estimated that if k_2 was the RDS, then $k_1 \gg k_2$, and k_2 can be set arbitrarily to be $k_1/10$ and $k_1/20$.[7]
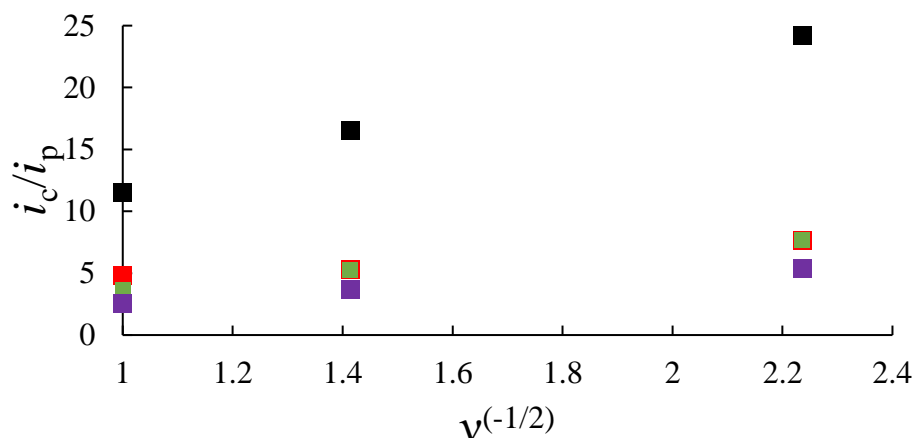
Figure 3.10. Experimentally and theoretically determined i_c/i_p for **1**. Black is the theoretical maximum for i_c/i_p, green is the experimental i_c/i_p measured from CVs, red is i_c/i_p calculated from $k_1/10$, and purple is i_c/i_p calculated from $k_1/20$.

Since the i_c/i_p values measured using the old technique are artificially low due to the non-ideal character of the wave, the theoretical maximum is instead given by FOWA back calculations of i_c/i_p from k_{cat}. An i_c/i_p above the region is theoretically impossible. Between the impossible region and above the arbitrary k_2 values lies the region in which k_1 can be said with confidence to be the rate determining step. Below k_2, no kinetic information can be gathered.[7] As seen in the above plot, for **1**, the experimental values are slightly above the theoretical maximum k_2 values, indicating that they are in the region between the maximum and k_2. This implies that k_2 is not rate limiting, and that k_1, which is much higher, is the rate determining step.[7] A calculation for **2** is also performed in Appendix B.

Supported by the literature technique, it is highly likely that $k_1 = k_{cat}$, which is the

universal rate constant in $M^{-1}s^{-1}$. For **1**, k_{cat} is 80,000 $M^{-1}s^{-1}$, and **2** is 20,000 $M^{-1}s^{-1}$. To

benchmark this against other catalysts, finding TOF_{max} in a 1 M solution of acid (TFA in our

case) yields a $k_{obs} = TOF_{max}$ of 80,000 s^{-1} for **1** and 20,000 s^{-1} for **2**.

Scan Rate ν (V/s)	Slope	R^2 of linear fit	k_{obs} (s^{-1}) at exptl. [H$^+$]	k_{obs} (s^{-1}) at 1 M [H$^+$]
0.2	18.86	0.99	230	75000
0.5	12.26	0.98	270	87000
1	8.48	0.98	260	85000

Table 3.2. Rate constants from FOWA of **1**.

Scan Rate ν (V/s)	Slope	R^2 of linear fit	k_{obs} (s^{-1}) at exptl. [H$^+$]	k_{obs} (s^{-1}) at 1 M [H$^+$]
0.2	8.33	0.99	27	31000
0.6	5.43	0.99	34	39000
1	3.96	0.99	30	39000

Table 3.3. Rate constants from FOWA of **2**.
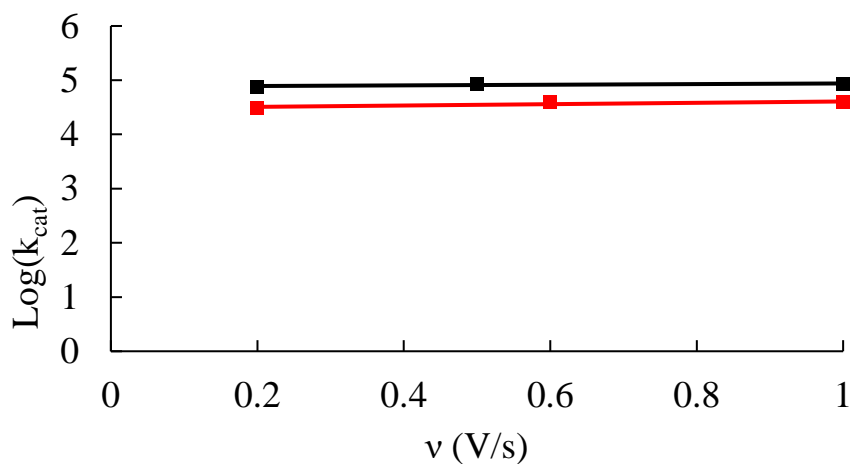
Figure 3.11. Rate constants k_{cat} of **1** (black) and **2** (red) plotted versus scan rate, indicating the rates are independent of scan rate.

In addition to the benchmarking values, the TOF corresponding to the experimental acid concentration is also reported. These values were calculated from the small, linear portion outlined in Figure 3.10. The resultant benchmarking TOF is quite high, indicating **1** and **2** are highly active cobalt catalysts for proton reduction. The TOF is also shown in Figure 3.12 to be independent of scan rate. These numbers correspond to the theoretically ideal behavior of the catalysts, if the electrochemical system was free of side phenomena. In addition to this kinetic information, it is of interest to incorporate overpotential into the electrocatalytic calculations for further benchmarking.

Tafel plots are a way to theoretically correlate TOF with overpotential. This is a useful benchmark because it allows for the visualization of the inverse relationship between activity and efficiency. Specifically, to benchmark the catalysts for comparison, Tafel plots can be used to calculate the TOF at 0 overpotential. This marks the TOF of the catalyst if it generated hydrogen at the reduction potential of a specific acid in a specific solvent.[7] The highest TOF at the lowest overpotential proves to be the most theoretically active and efficient catalyst. Overpotential (η) is similarly defined compared to the previous definition, but it incorporates the sweeping potential scan in its use of E rather than the half wave potential. η is the relationship between this varying potential and the value E^0_{H+/H_2}, which is a reference value that is calculated using the pKa of an acid in a specific solvent.[7]

$$\eta = E^0_{H+/H_2} - E$$

E^0_{H+/H_2} can be calculated from literature values.[8] Nocera and coworkers report this value for 1 M TFA in CH$_3$CN to be $E^0_{H+/H_2} = $ -0.62 V vs. Fc$^+$/Fc.[8] As mentioned in the introduction, this can

then be put into the equation:

$$TOF = \frac{TOF_{max}}{1 + e^{\left(\frac{F}{RT}\right)\left(E^0_{H+/H_2} - \eta - E_{Redox}\right)}}$$

A Tafel plot is then generated.
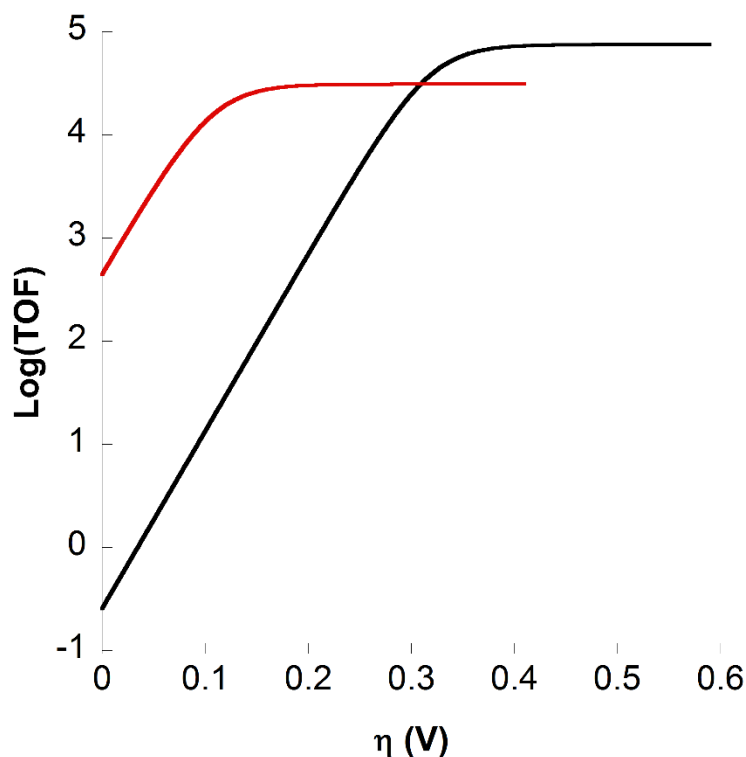
Figure 3.12. Tafel plot of **1** (black) **2** (red) at v = 200 mV/s.

The TOF of **1** is higher at its leveled overpotential, however its plateau is reached at a

larger η than **2**. This implies that while **1** is a more active catalyst by a whole order of

magnitude, **2** is more efficient energetically by approximately 200 mV. Interestingly, **2** has a

larger TOF at 0 overpotential. However, Tafel plots are not thought to be extremely accurate,

and kinetic information calculated through FOWA is therefore more valuable overall.[4]

To ensure homogeneity, and to ensure the activity of the catalyst is as reported, control

studies were performed. Dip tests for homogeneity showed that, even when the electrodes were

not polished, that a previous experiment does not influence the current CV by carrying out a

controlled version of that situation. If the solution was heterogeneous, it would be likely that the heterogeneous catalyst would influence the new scan. It was shown that no such catalytic response occurred for **1** or **2** (see Appendix B). In addition to examining homogeneity, background scans of just TBAPF$_6$ and just TBAPF$_6$ and TFA showed that there was no reduction peak of TFA present in the region in which our catalysts reduce protons to hydrogen (see Appendix B). This suggests that our catalyst was the only molecule responsible for the current increases.

Active and cost-effective derivatives of asymmetric Schiff base cobalt complexes with low overpotentials have been reported for proton reduction. With the use of FOWA and Tafel plots, the accuracy of the electrochemical analysis of the complexes increased, and the complexes can now be compared to other modern electrocatalysts.

References

1. Hu, X., Brunschwig, B., & Peters, J. (2007). Electrocatalytic hydrogen evolution at low overpotentials by cobalt macrocyclic glyoxime and tetraimine complexes. *J. Am. Chem. Soc., 129*(29), 8988-98.
2. Mcnamara, W., Han, Z., Alperin, P., Brennessel, W., Holland, P., & Eisenberg, R. (2011). A cobalt-dithiolene complex for the photocatalytic and electrocatalytic reduction of protons. *J. Am. Chem. Soc.*, 133(39), 15368-71.
3. Armstrong, J., Crossland, P., Frank, M., Van Dongen, M., & Mcnamara, W. (2016). Hydrogen evolution catalyzed by a cobalt complex containing an asymmetric Schiff-base ligand. *Dalton Trans*., 45(13), 5430-5433.
4. Rountree, E., Mccarthy, B., Eisenhart, T., & Dempsey, J. (2014). Evaluation of homogeneous electrocatalysts by cyclic voltammetry. *Inorg. Chem*., 53(19), 9983-10002.
5. G. P. Connor, K. J. Mayer, C. S. Tribble, and W. R. McNamara. (2014). Hydrogen Evolution Catalyzed by an Iron Polypyridyl Complex in Aqueous Solutions. *Inorg. Chem.* **2014,** 53 (11), 5408-5410.
6. Costentin, C., Drouet, S., Robert, M., & Savéant, J. (2012). Turnover numbers, turnover frequencies, and overpotential in molecular catalysis of electrochemical reactions. Cyclic voltammetry and preparative-scale electrolysis. *J. Am. Chem. Soc.*, 134(27), 11235-42.
7. Elgrishi, N., Chambers, M., & Fontecave, M. (2015). Turning it off! Disfavouring hydrogen evolution to enhance selectivity for CO production during homogeneous CO2 reduction by cobalt– terpyridine complexes. *Chem. Sci.* 6, 2522
8. Maher, A., Passard, G., Dogutan, D., Halbach, R., Anderson, B., Gagliardi C., Taniguchi, M., Lindsey, J., & Nocera, D. (2017). Hydrogen Evolution Catalysis by a Sparsely Substituted Cobalt Chlorin. *ACS Catal*. 7, 3597-3606.
9. APEX3, version 2016.5-0; Bruker AXS: Madison, WI, 2016.
10. Sheldrick, G. M. SADABS, version 2016/2; J. Appl. Cryst. 2015, 48, 3-10.
11. SAINT, version 8.34A; Bruker AXS: Madison, WI, 2013.
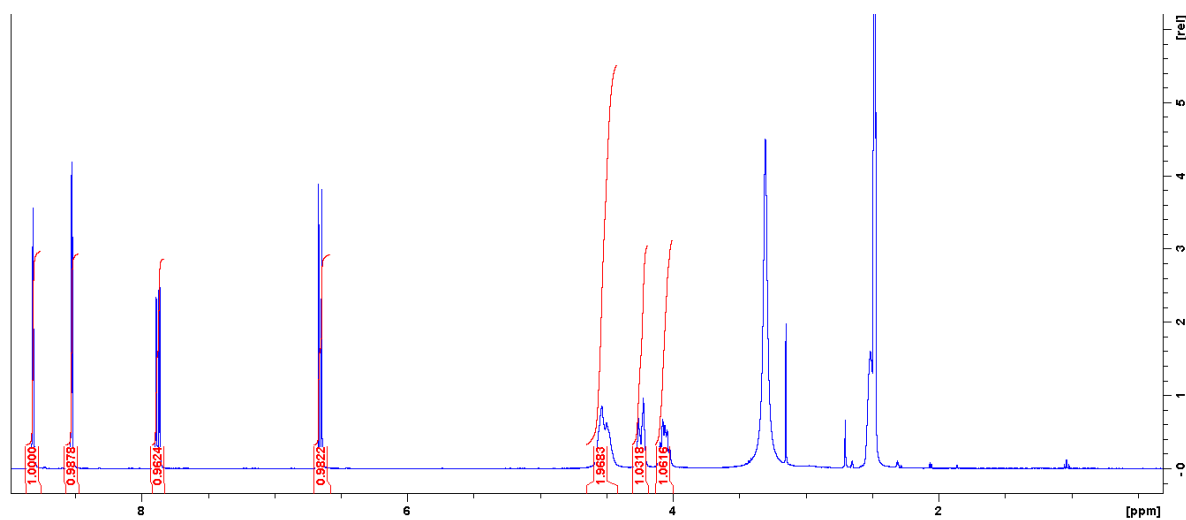
Figure B1. ^{1}H NMR of **1** with integrations
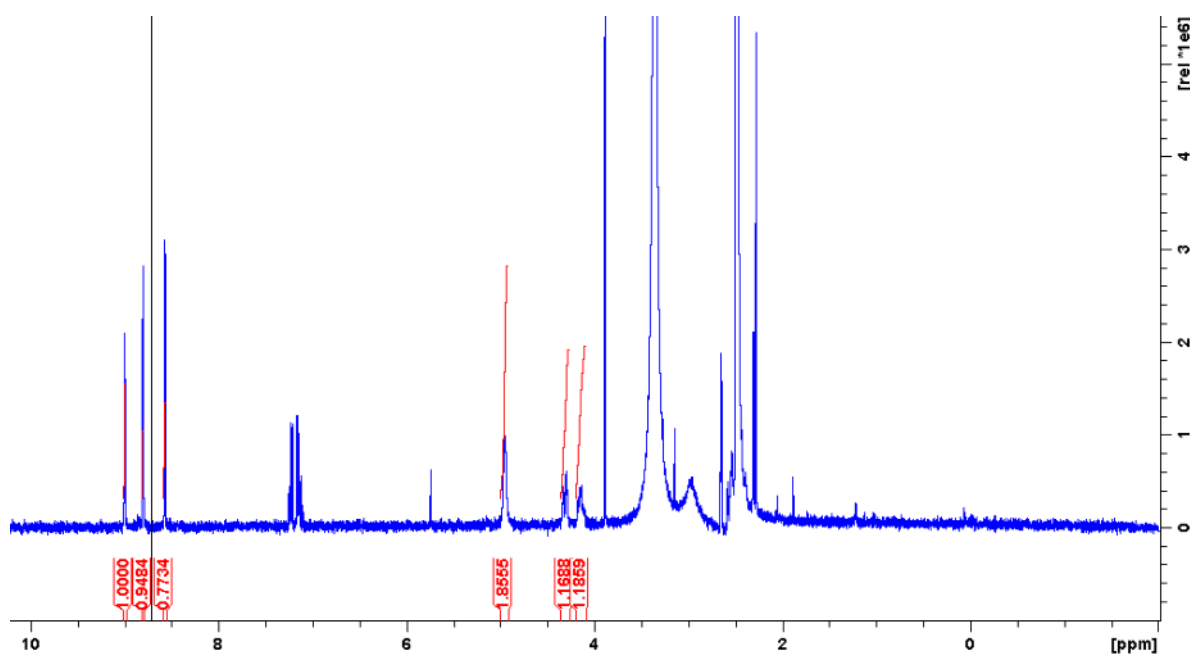
Figure B2. ^{1}H NMR of **2** with integrations.
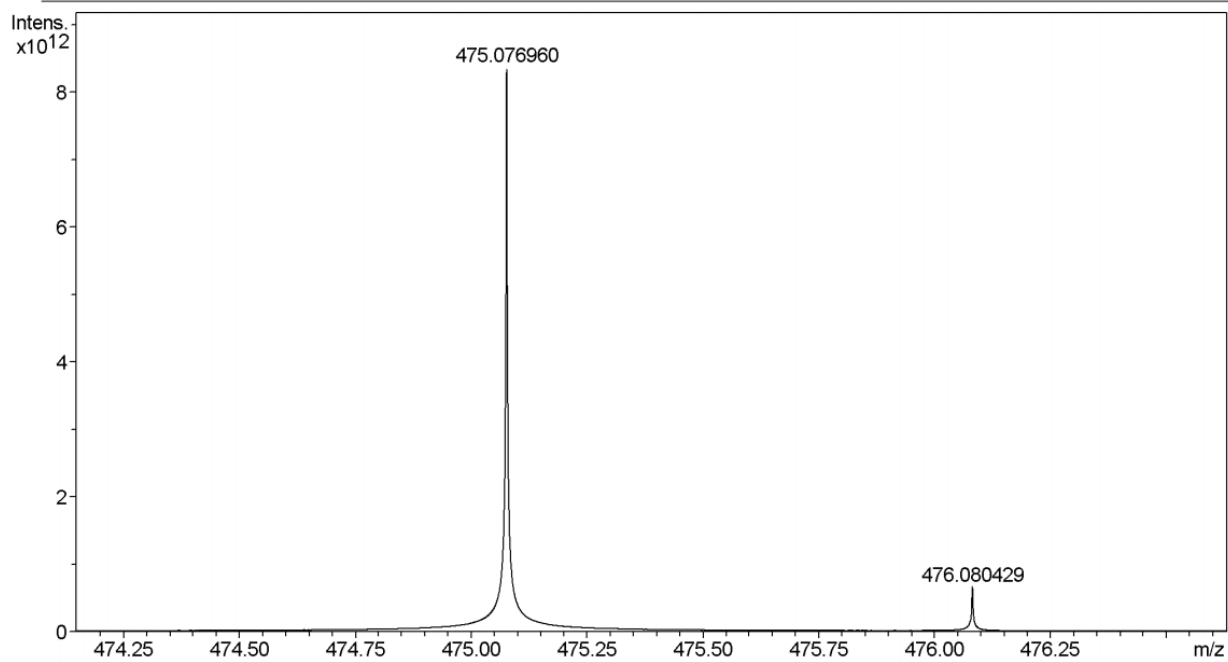
Figure B3. Mass spectrum of **1**. The peak matches the predicted molecular weight.
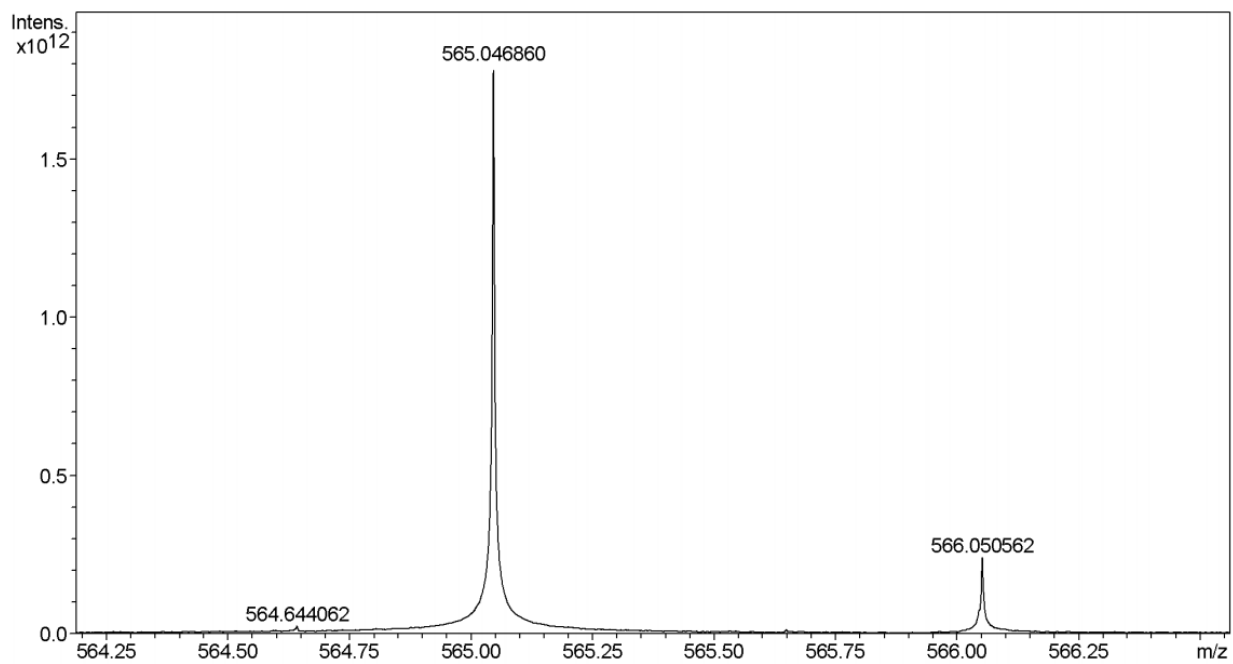
Figure B4. Mass spectrum of **2.** The peak matches the predicted molecular weight.
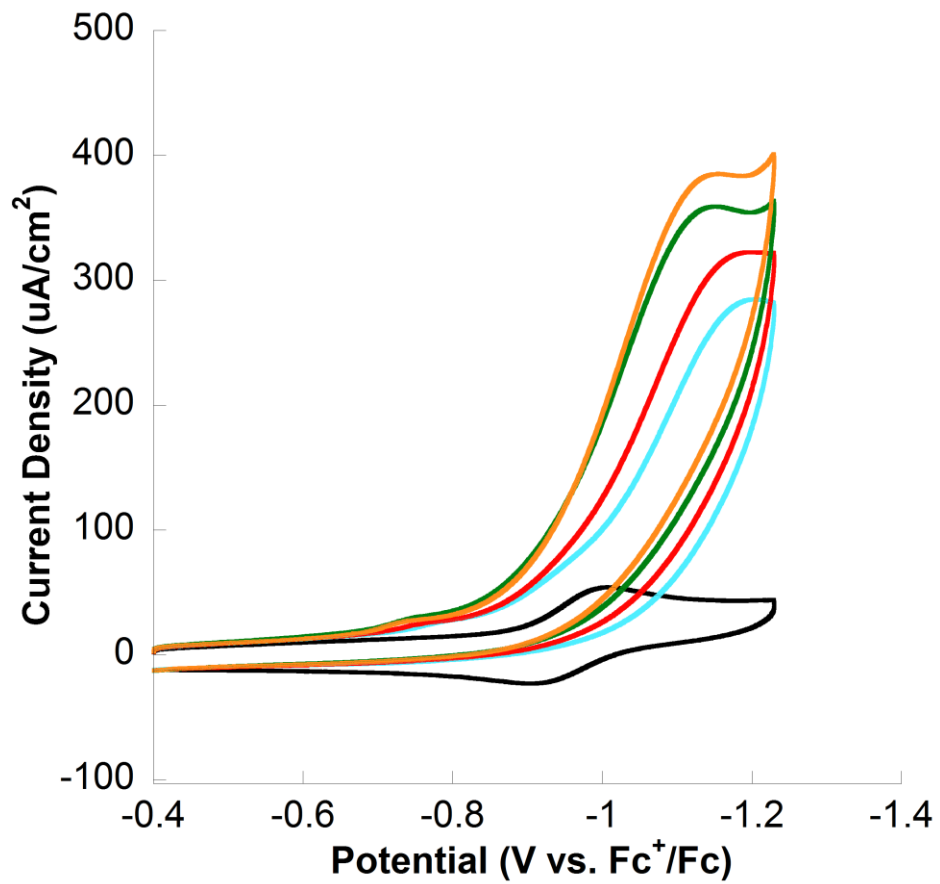
Figure B5. CV of 0 mM (black), 0.88 mM (blue), 1.76 mM (red), 2.42 mM (green), 3.08 mM (orange) of TFA with **1** at ν = 200 mV/s.
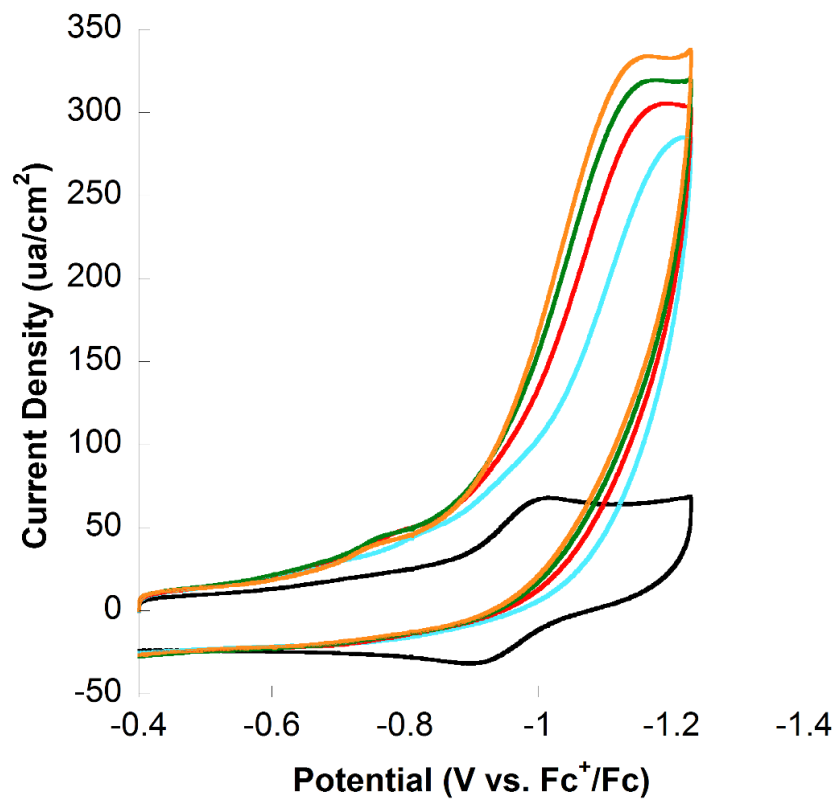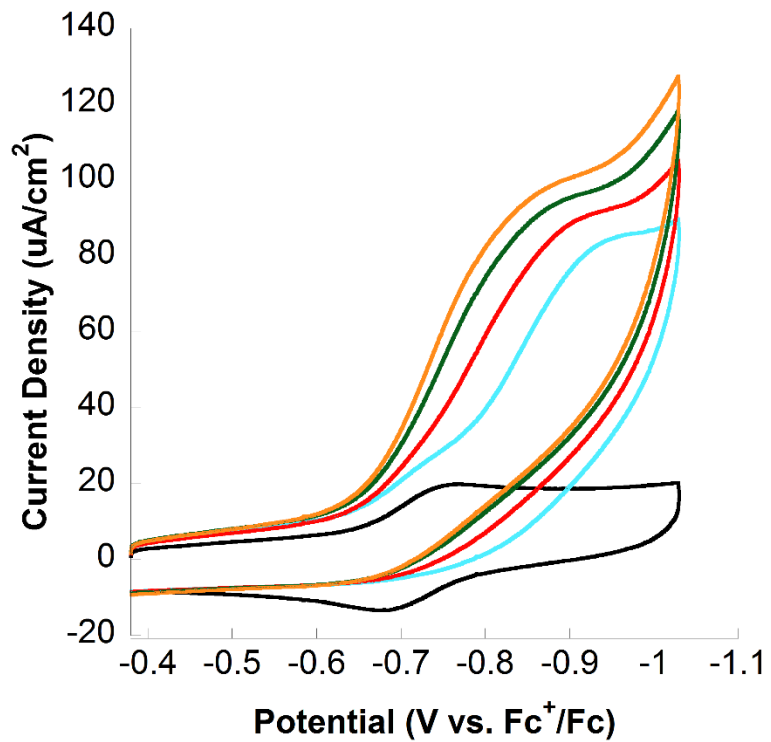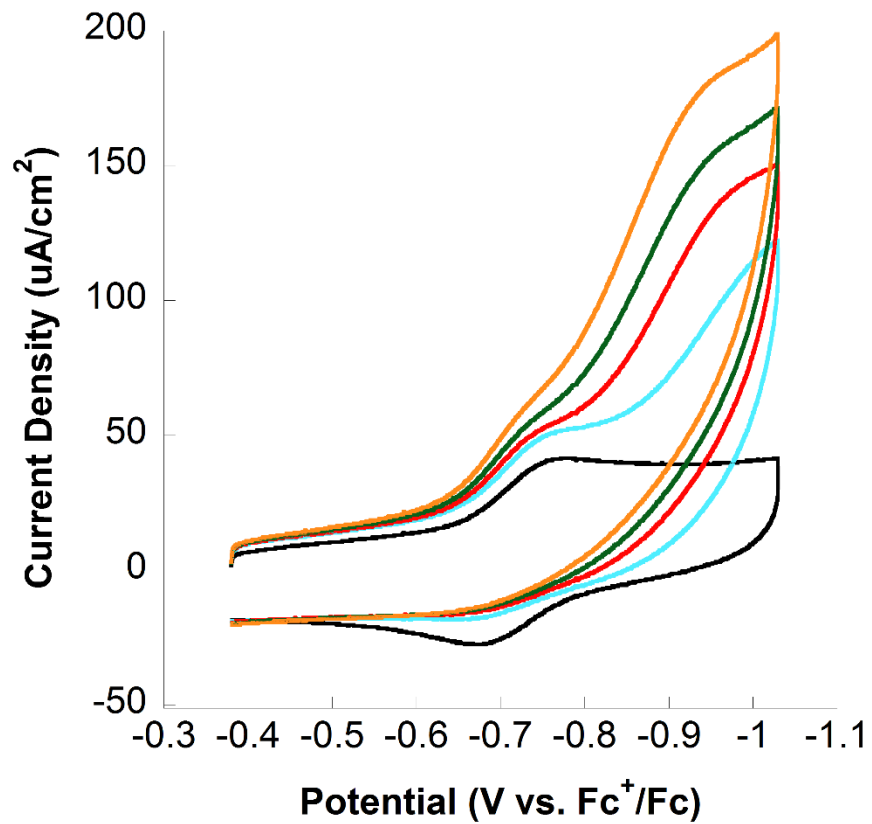
Figure B6. CV of 0 mM (black), 0.88 mM (blue), 1.76 mM (red), 2.42 mM (green), 3.08 mM (orange) of TFA with **1** at ν = 500 mV/s.

Figure B7. CV of 0 mM (Black), 0.22 mM (Blue), 0.44 mM (Red), 0.66 mM (Green), and 0.88 mM (Orange) of TFA with **2** at $\nu = 200$ mV/s.
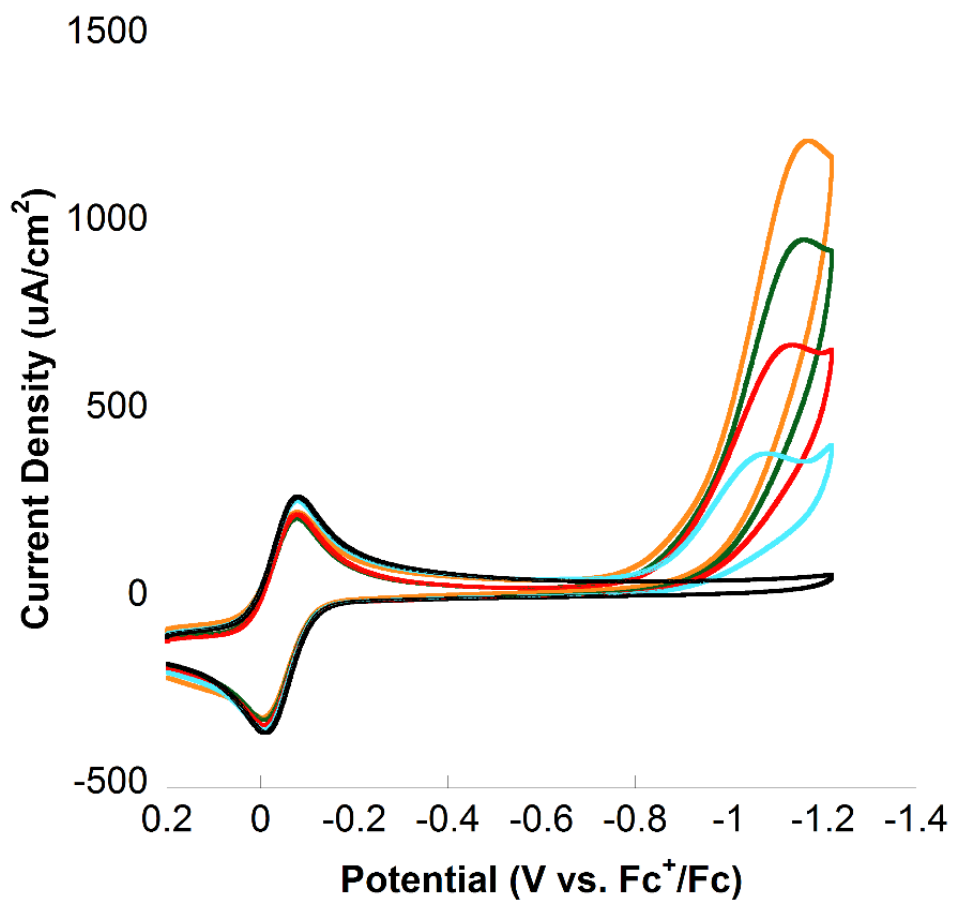
Figure B8. CV of 0 mM (Black), 0.22 mM (Blue), 0.44 mM (Red), 0.66 mM (Green), and 0.88 mM (Orange) of TFA with **2** at $\nu = 600$ mV/s.
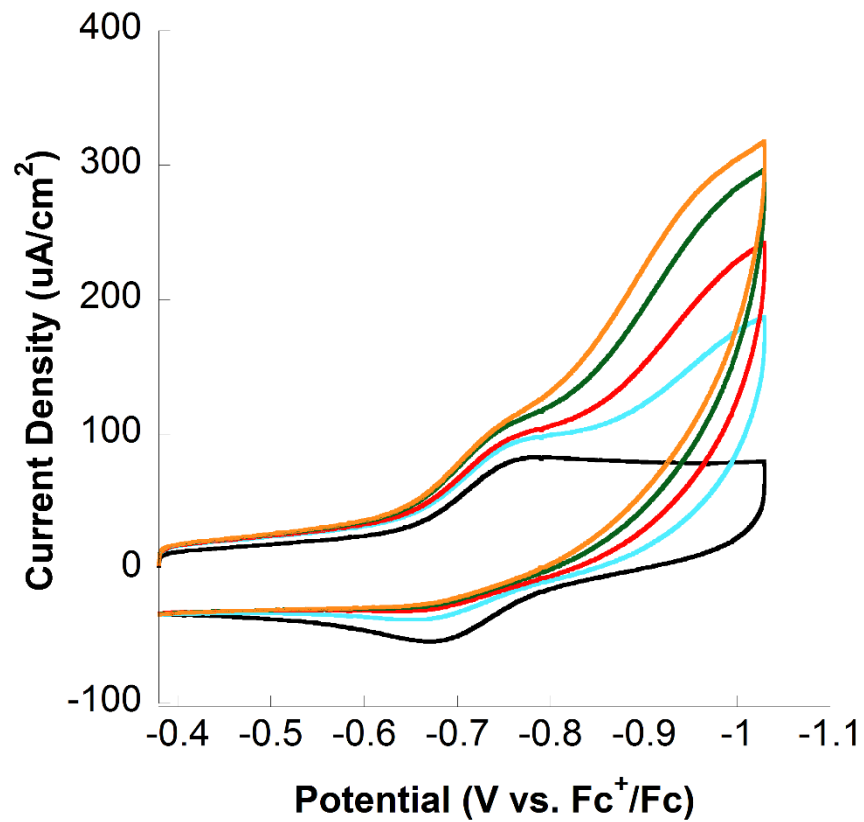
Figure B9. CV of 0 mM (Black), 0.22 mM (Blue), 0.44 mM (Red), 0.66 mM (Green), and 0.88 mM (Orange) of TFA with **2** at ν = 1 V/s
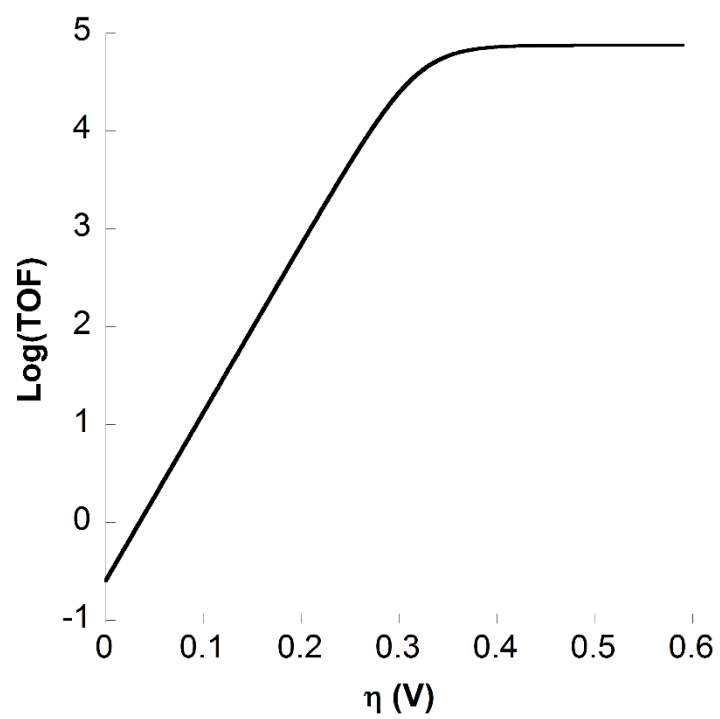
Figure B10. Tafel plot of **1** at ν = 200 mv/s
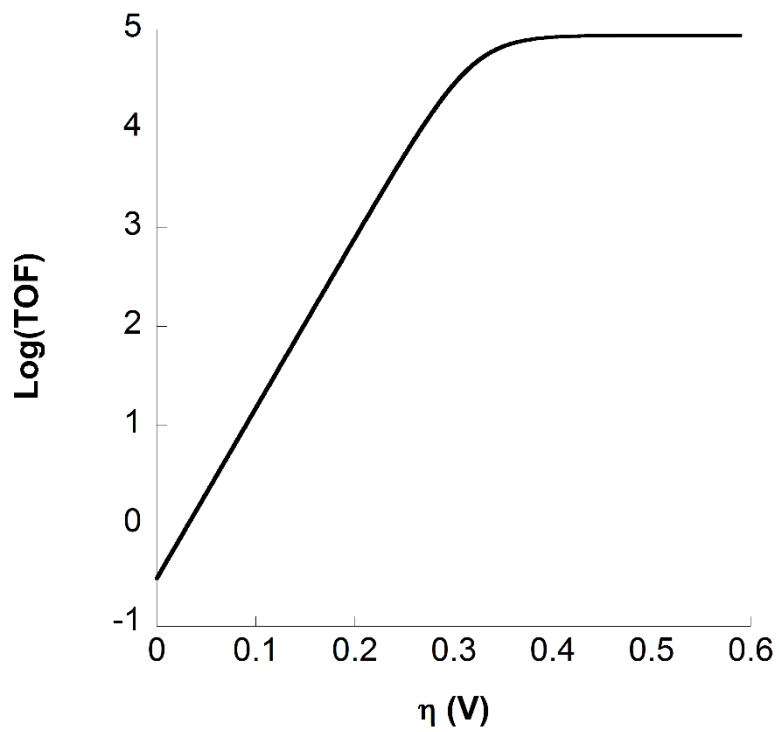
Figure B11. Tafel plot of **1** at ν = 500 mv/s
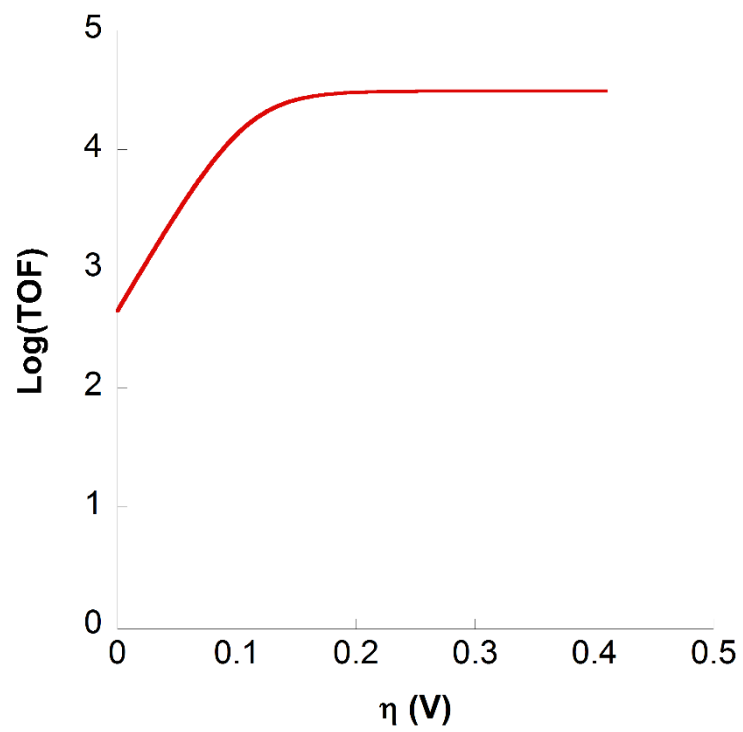
Figure B12. Tafel plot of **2** at ν = 200 mv/s
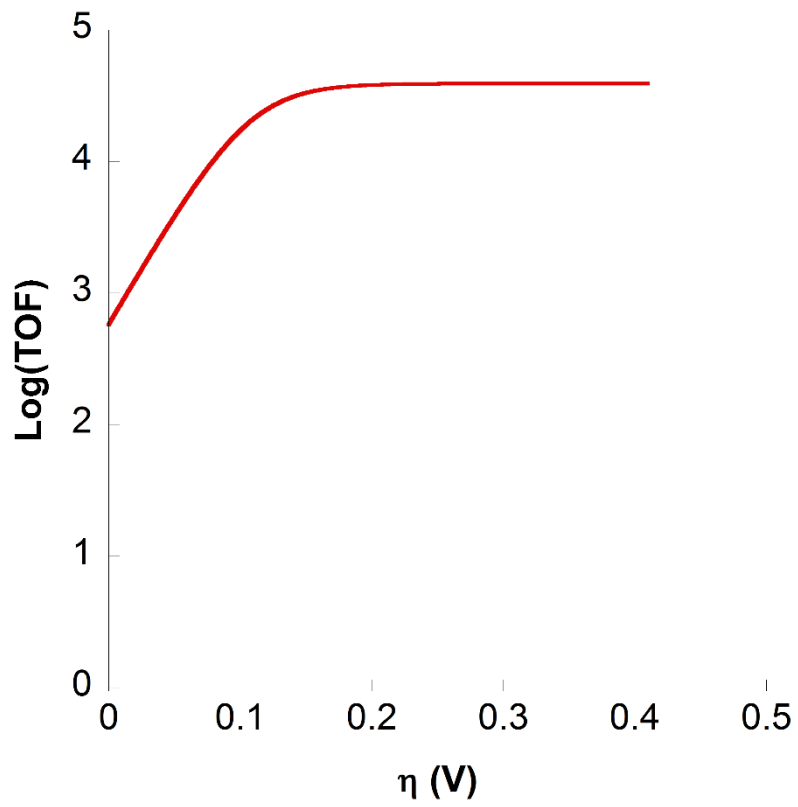
Figure B13. Tafel plot of **2** at ν = 600 mV/s
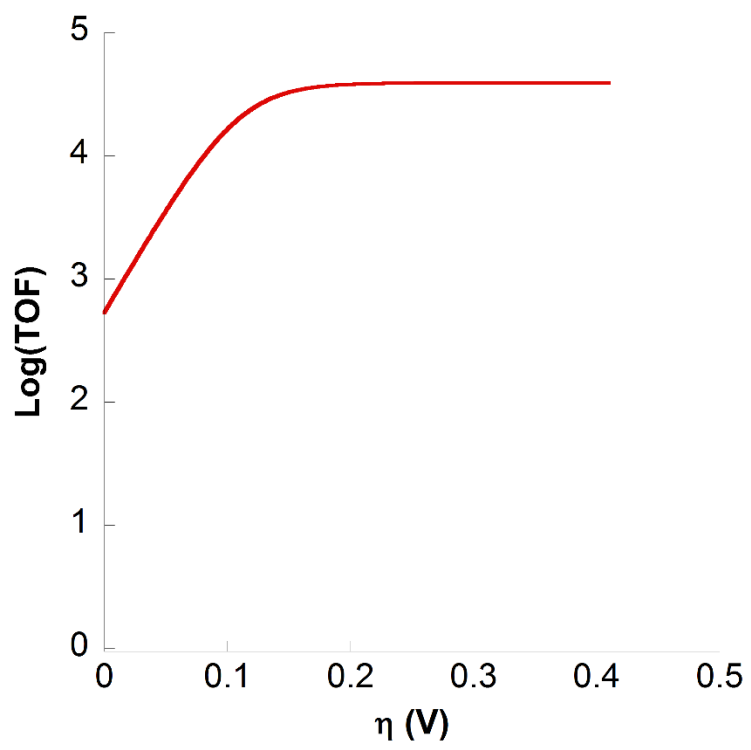
Figure B14. Tafel plot of **2** at ν = 1 V/s
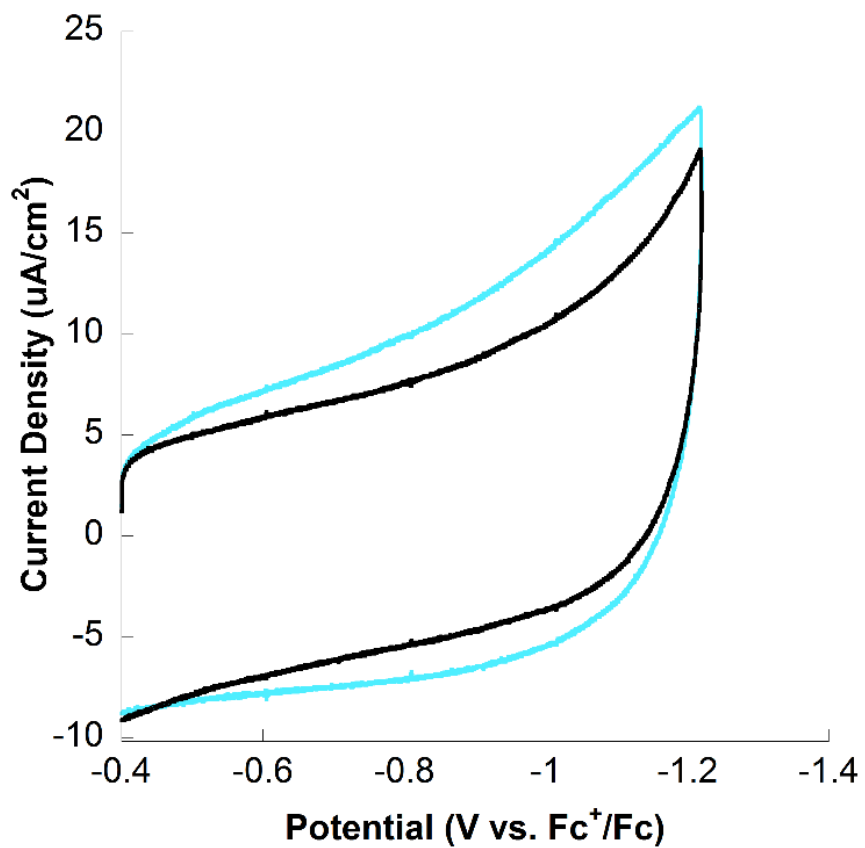
Figure 15. Background scan in the region of **1**'s scans with TBAPF$_6$ in CH$_3$CN (Black) and addition of TFA (Blue).
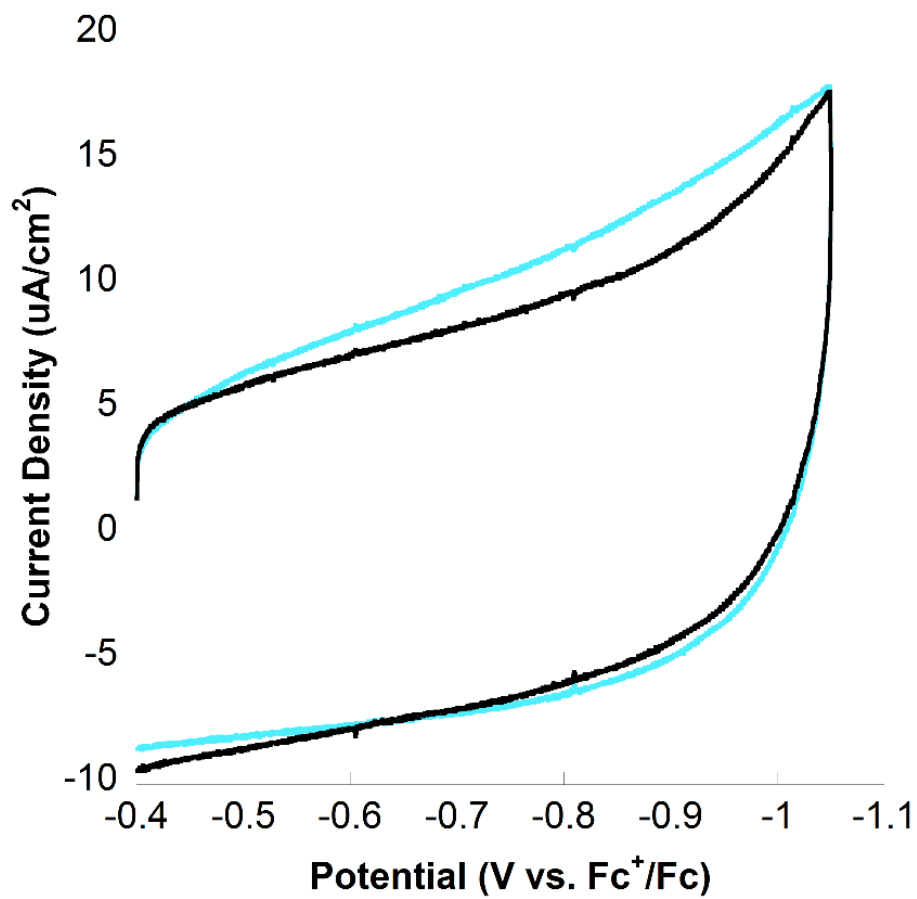
Figure 16. Background scan in the region of **2**'s scans with TBAPF$_6$ in CH$_3$CN (Black) and addition of TFA (Blue).

Figure B17. CV of 0 mM (Black), 0.2 mM (Blue), 0.4 mM (Red), 0.6 mM (Green), and 0.8 mM (Orange) of **1** with 44 mM TFA at ν = 200 mV/s.
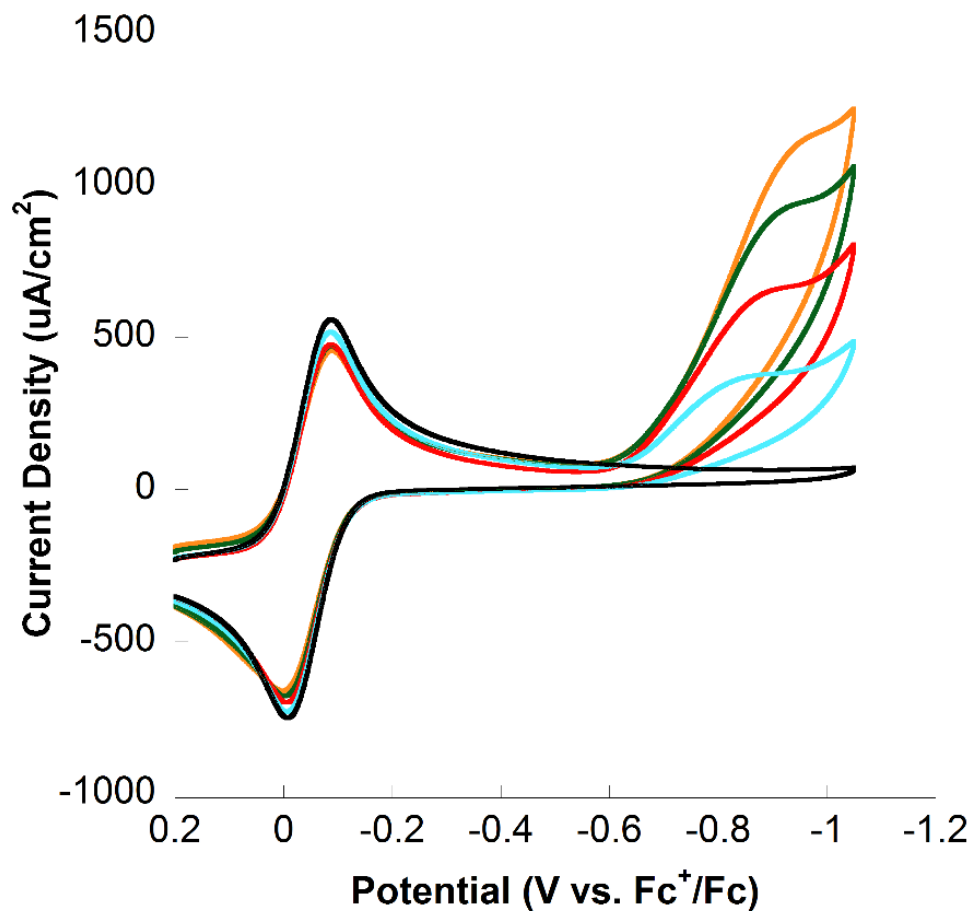
Figure B18. CV of 0 mM (Black), 0.2 mM (Blue), 0.4 mM (Red), 0.6 mM (Green), and 0.8 mM (Orange) of **2** with 44 mM TFA at ν = 200 mV/s.
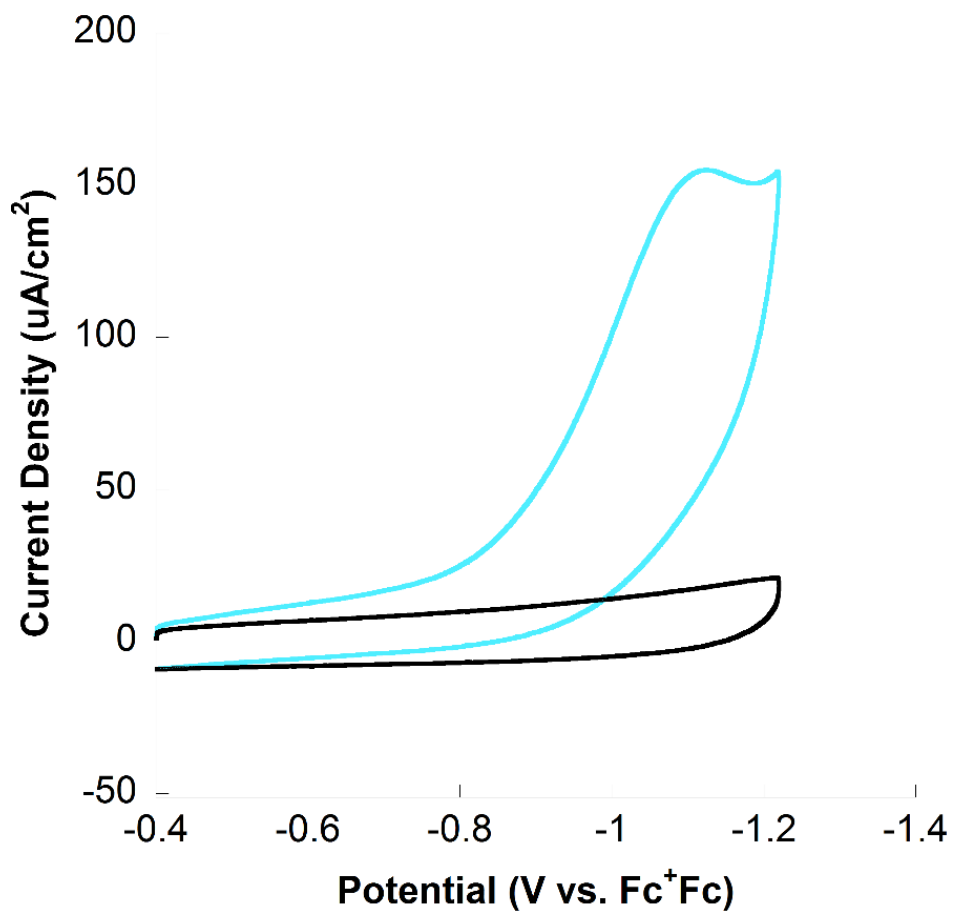
Figure B19. Dip test of **1**. Scan of 0.1 M TBAPF$_6$, 8.8 mM TFA with **1** in 5 mL CH$_3$CN (blue) and a subsequent scan of 0.1 M TBAPF$_6$ in 5 mL CH$_3$CN without polishing the electrodes.
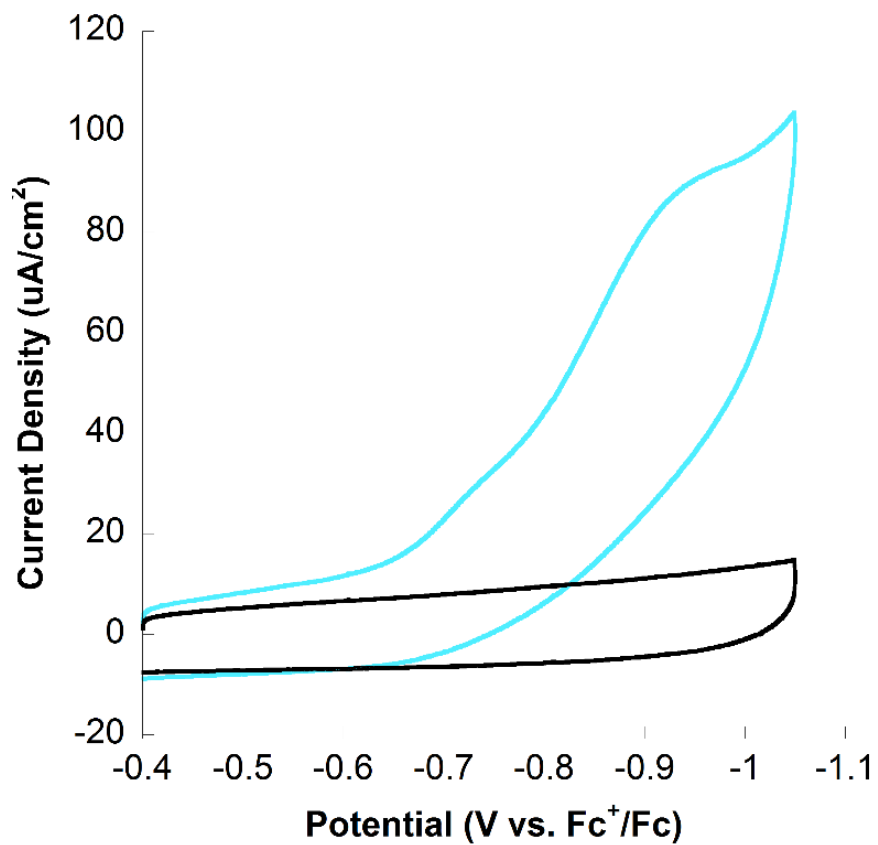
Figure B20. Dip test of **2**. Scan of 0.1 M TBAPF$_6$, 8.8 mM TFA with **2** in 5 mL CH$_3$CN (blue) and a subsequent scan of 0.1 M TBAPF$_6$ in 5 mL CH$_3$CN without polishing the electrodes.
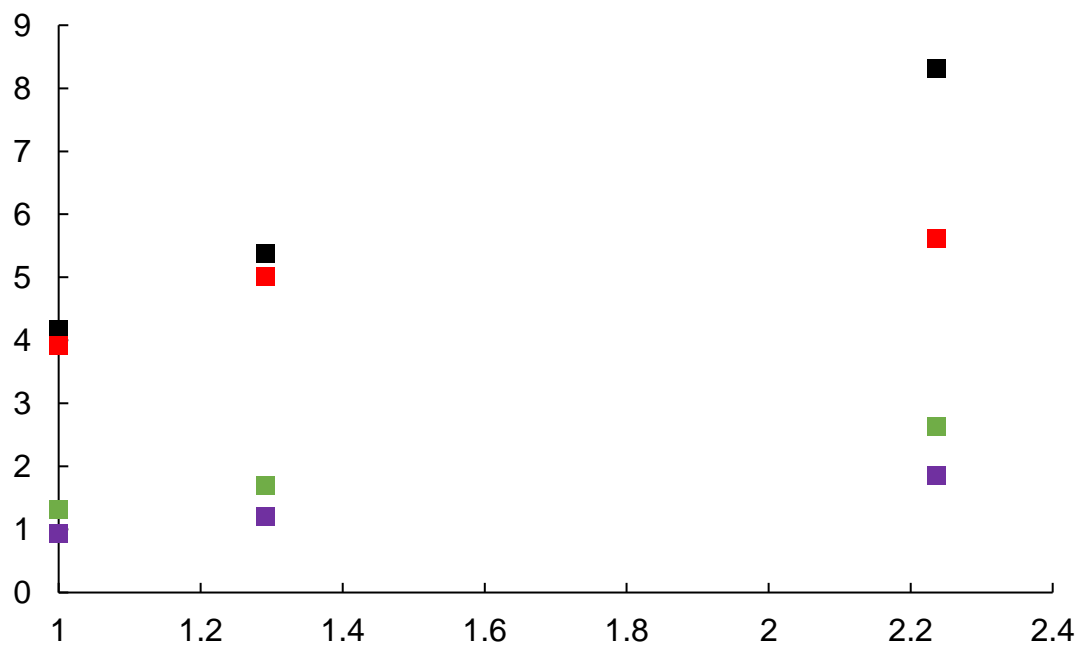
Figure B21. i_c/i_p analysis for RDS for **2**. Red is the experimentally measured i_c/i_p, black is the theoretical maximum for k_{cat}, green is $k_1/10$, and purple is $k_1/20$. This indicates that the rate determining step is k_1, meaning that $k_1=k_{cat}$ for **2**.[7]